Evolution of Kelvin-Helmholtz activity on the dusk flank magnetopause

C. Foullon,[1] C. J. Farrugia,[2] A. N. Fazakerley,[1] C. J. Owen,[1] F. T. Gratton,[3] and R. B. Torbert[2]

[1]   Our purpose is to characterize the evolution of the magnetopause Kelvin-Helmholtz (KH) wave activity with changes in thickness of the adjacent boundary layer, geomagnetic latitude and interplanetary magnetic field (IMF) orientation. As the IMF turns northward, wave activity may be generated at the dayside before propagating down the tail, where the boundary layer is expected to support longer wavelengths. We use two-point observations on the dusk magnetopause at low latitudes, from *Geotail* on the dayside and *Cluster* tailward of the dusk terminator. We quantify the wavelength, power, wavefront steepness and propagation direction at *Cluster*. An estimate of the thickness of the low-latitude boundary layer (LLBL) is obtained by correlating normal distances to the magnetopause, derived from two empirical solar-wind-driven models, with a systematic relationship (the "transition parameter") found between the electron number density and temperature; the correlation factor is used to infer the temporal evolution of the thickness of the locally sampled layer. We find that wavelengths are controlled by the IMF clock angle, as expected when generated by the KH mechanism at the dayside, although amplitudes, wavefront steepness and propagation directions are more closely correlated with the layer thickness. A survey of parameter space provides evidence of the contribution of the KH mechanism to the widening of the electron LLBL.

1.   Introduction

[2]   The outer boundary of the Earth's magnetosphere, the magnetopause, and its adjacent boundary layers are continually in motion, the main cause of which are pressure variations in the shocked solar wind plasma impinging on this boundary. The motions may also be due to the action of local instabilities, such as the Kelvin-Helmholtz (KH) instability driven by flow shears, which excite surface waves [e.g., *Kivelson and Chen*, 1995; *Farrugia et al.*, 2001]. Whatever their cause, these boundary motions in turn generate compressional magnetohydrodynamic (MHD) waves that propagate into the magnetosphere and sometimes excite resonances on field lines that can support waves with comparable frequencies [e.g., *Hughes*, 1981]. The boundary motions may play a role in plasma entry to the magnetosphere, a central concern in magnetospheric physics. Generally, when the interplanetary magnetic field (IMF) is southward and a large magnetic shear exists between the geomagnetic field and the IMF, the process of magnetic reconnection is recognized as the main contributor to plasma exchange across the dayside subsolar magnetopause [*Dungey*, 1961]. However, when the IMF is northward, the situation is less clear. There are several proposed entry mechanisms, including (1) diffusive entry [e.g., *Treumann et al.*, 1995; *Terasawa et al.*, 1997], (2) lobe reconnection occurring in one or both hemispheres [e.g., *Song et al.*, 2002; *Bogdanova et al.*, 2005] and (3) the KH instability. Although the latter mechanism has been investigated on multiple levels of time-dependent simulations [e.g., *Miura*, 1984; *Wu*, 1986; *Manuel and Samson*, 1993; *Thomas and Winske*, 1993; *Fujimoto and Terasawa*, 1994], it needs a violation of the frozen-in law or magnetic reconnection triggered in KH vortices [e.g., *Otto and Fairfield*, 2000]. Issues intimately connected with this debate include the formation under northward IMF of the low-latitude boundary layer (LLBL) [e.g., *Eastman et al.*, 1976] and the origin of the cold dense plasma sheet [e.g., *Øieroset et al.*, 2002].

[3]   KH waves are commonly understood as surface waves, characterized by a rapid spatial decay away from both sides of the interface. In the simplest linear MHD description, the onset condition for the KH instability in an ideal incompressible plasma, with a discontinuous velocity

[1]Mullard Space Science Laboratory, University College London, Surrey, UK.
[2]Space Science Center and Department of Physics, University of New Hampshire, Durham, New Hampshire, USA.
[3]Instituto de Física del Plasma, CONICET, Universidad de Buenos Aires, Buenos Aires, Argentina.
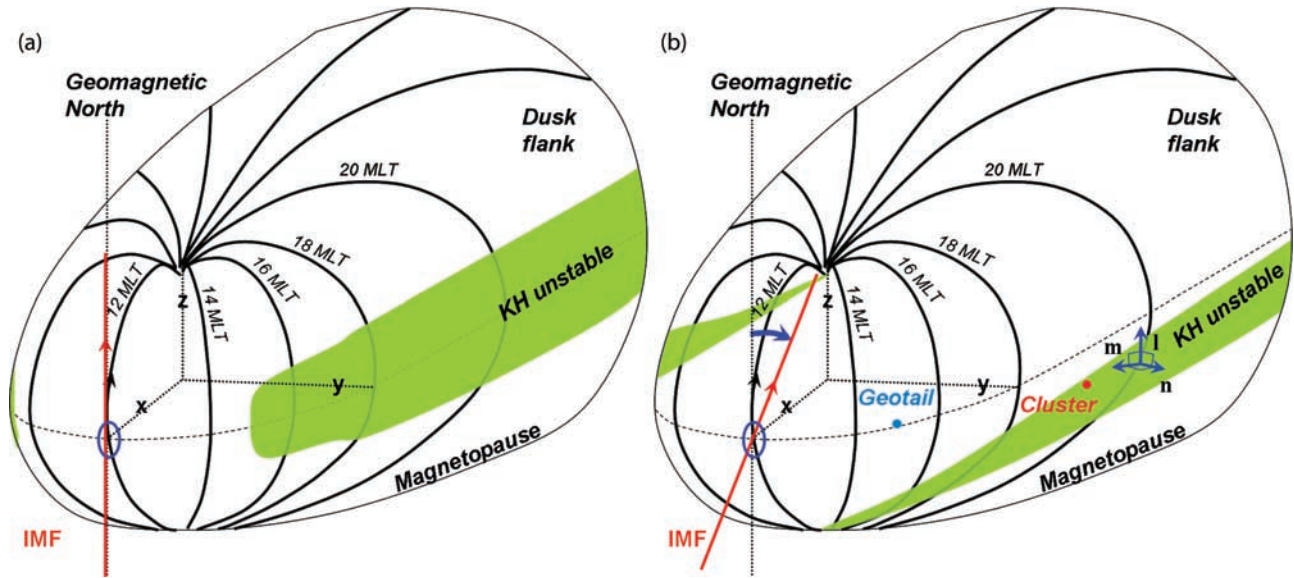
Figure 1. View of the magnetopause and adjacent geomagnetic field from a dayside and North-East vantage point. The distribution in green of KH unstable regions is given for maximum KH growth rates above a 0.1 threshold as obtained without boundary layer by F98 for northward IMF with (a) zero IMF clock angle and (b) an IMF clock angle (indicated by a blue arc) of 30°. Slightly reduced growth rates are obtained in the presence of the boundary layer. The regions of instability represented on the nightside are an extension (downtail) of the regions that are validated by the simulation results of F98 on the dayside. In Figure 1b, positions of *Geotail* and *Cluster* on the dusk flank are indicated in blue and red filled circles, respectively; a boundary normal coordinate system (**l**, **m**, **n**) is shown for illustration.

shear layer and assuming the layer to be infinitely thin (i.e., in the limit of no boundary layer or long wavelengths) [*Talwar*, 1964], is

$$[\mathbf{k}.(\mathbf{V_1} - \mathbf{V_2})]^2 > \frac{n_1 + n_2}{\mu_0 m_p n_1 n_2}\big[(\mathbf{k}.\mathbf{B_1})^2 + (\mathbf{k}.\mathbf{B_2})^2\big]. \quad (1)$$

Here the indices refer to the two plasma environments on either side of the boundary, n is the plasma number density, m_p the proton mass, μ_0 the permeability of free space, $\mathbf{V}$ is the plasma flow velocity, $\mathbf{B}$ the magnetic field vector and $\mathbf{k}$ the wave vector; $\mathbf{V}$, $\mathbf{B}$ and $\mathbf{k}$ are all tangential to the layer. As equation (1) shows, KH waves are caused by a velocity gradient or shear, $|\mathbf{V_1} - \mathbf{V_2}|$, between the streaming magnetosheath and relatively stagnant magnetospheric plasmas, in the case of the magnetopause. The instability criterion is more likely to be met for wave propagation in the direction of high flow shear. Moreover, the threshold above which KH instability may occur (i.e., the right-hand side in equation (1)) is reduced in the regions of low or high magnetic shear, between the magnetosheath and magneto-spheric field lines and for wave propagation perpendicular to the magnetic fields: this part corresponds to stabilizing effects from magnetic tension forces [e.g., *Chandrasekhar*, 1961] that are weakened for strongly northward or southward IMF.

[4] Figure 1 illustrates the relation between the regions satisfying the conditions for the KH instability onset, i.e., wave activity generation, and the IMF clock angle, defined as the polar angle of the IMF direction in the Geocentric Solar Magnetospheric (GSM) YZ plane. This figure is adapted from *Farrugia et al.* [1998], hereafter F98, who performed linear MHD simulations of the incompressible surface mode disturbances on a mesh covering the dayside of a model magnetopause. Regions of maximum KH growth rates on the dayside magnetopause correspond, as expected, to regions of high flow shear and low magnetic shear. The wave perturbations may become unstable away from the stagnation point in the direction of high flow shear. For small clock angle, the regions of maximum KH growth rates are broad and confined to the equator away from the sunward side (Figure 1a). As the clock angle increases in absolute value (the case of positive clock angle is represented in Figure 1b), the regions of instability narrow and migrate away from the equator, southward on one flank and northward on the other, depending on the sign of the clock angle.

[5] However, even the most advanced linear models predict initial growth at wavelengths that are shorter than the wavelengths of a few 10^4 km typically observed on the magnetopause [see, e.g., *Belmont and Chanteur*, 1989, for a review]. The commonly accepted solution to this discrepancy is that convectively unstable KH surface waves grow, in both amplitude and wavelength, while propagating down the tail, until they become nonlinear, break into turbulence and roll-up into vortices. For example, *Gustafsson et al.* [2001] and *Owen et al.* [2004] report the steepening of waves along the flank magnetopause, which can be interpreted as evidence of KH waves in their growing phase [*de Keyser*, 2005]. In addition, *Fairfield et al.* [2000] and *Hasegawa et al.* [2004] report structures with vortical plasma flow, strong twisting of the magnetic field and a

Table 1. Instruments Providing Magnetic Field and Plasma In-Situ Measurements

Mission	Magnetic Field	Plasma
ACE	Magnetic Fields Experiment (MAG) [*Smith et al.*, 1998]	Solar Wind Electron Proton Alpha Monitor (SWEPAM) [*McComas et al.*, 1998]
Geotail	Magnetic Field investigation (MGF) [*Kokubun et al.*, 1994]	Solar Wind Analyzer (SWA) from the comprehensive plasma instrument (CPI) [*Frank et al.*, 1994]
Cluster	Flux Gate Magnetometer (FGM) [*Balogh et al.*, 2001]	Plasma Electron and Current Experiment (PEACE) [*Johnstone et al.*, 1997]; *Cluster* Ion Spectrometry (CIS) experiment [*Rème et al.*, 2001]; Electric Fields and Waves (EFW) [*Gustafsson et al.*, 2001]

filament-like high-density plasma region intruding into the low-density (magnetospheric) environment.

[6] Moreover, it is not clear whether, and to what extent, the KH mechanism generates the observed properties of the LLBL, a mixing layer adjacent to and Earthward of the magnetopause at low geomagnetic latitudes, with densities and velocities intermediate between values in the magnetosheath and the proper magnetosphere. These properties may result, for example, from diffusion onto closed field lines [e.g., *Phan et al.*, 1997] or reconnection of interplanetary and geomagnetic fields [e.g., *Lockwood and Hapgood*, 1997]. Both particle transport mechanisms may operate in KH vortices, which may then carry the mixed plasma over large distances down the tail [*Otto and Fairfield*, 2000].

[7] Theoretical studies of the KH instability using ideal MHD are relevant to understanding the source and the nonlinear development of the waves. In the non-linear stage, numerical simulations [e.g., *Miura*, 1999a, 1999b] predict that fast growth of KH waves or vortices with smaller wavelengths or length scales results in the early saturation of those structures. The simulated small-scale vortices resulting from the instability near the subsolar magnetopause merge and evolve into large-scale vortices on the distant tail magnetopause. As a result, the spectrum of KH waves or vortices is expected to change along the magnetospheric boundary, in a so-called "inverse cascade", with the later evolution dominated by the largest length scales [*Belmont and Chanteur*, 1989]. In particular, simulations of the KH non-linear development with time obtain an almost linear relationship between the dominant wavelength (or length scale) and time since the initial perturbations [*Miura*, 1999a].

[8] The non-linear development is a function of time and, for a propagating wave, of space. Therefore changes in wavelengths, observed by a spacecraft at a fixed location along the magnetospheric boundary, can be caused either by different amplitudes of the upstream perturbation or changing distances from the upstream sources [*Otto and Fairfield*, 2000]. *Miura* [1999a] used observations from different events, i.e., with different equilibrium conditions, to obtain the regression fit $\tau = 10 R_s + 61.7$ between magnetopause periodicities (or repetition times), τ [s], and the distance, R_s [R_E], along the magnetopause from the subsolar point.

[9] However, the source regions of KH waves may vary in position from one case to the next, due to the influence of the global magnetospheric geometry, i.e., its shape and the changes of plasma and field conditions along the boundary (e.g., Figure 1 and F98). The influence of this factor on the properties of KH waves has not received much attention to date. Using records from ground magnetometer chains,

Farrugia et al. [2000, see their Figure 12] have shown an inverse dependence between the geomagnetic pulsation period and the IMF clock angle. A similar dependency between the degree of wave activity at the flank and the IMF clock angle remains to be tested. Neglecting upstream variations of the solar wind speed and density, we will demonstrate that changes in IMF clock angle may give rise to wavelength changes along the magnetospheric boundary. We will also examine whether this degree of wave activity can be related to the overall formation of the LLBL.

[10] We study an event on the 20 and 21 November 2001, when an exceptionally prolonged observation of wave activity is made at *Cluster*. This has been interpreted as showing evidence of rolled-up KH vortices [*Hasegawa et al.*, 2004]. We use widely separated observations at low latitudes on the dusk flank magnetopause, from *Geotail* on the dayside and *Cluster* tailward of the dusk terminator, during a period of northward IMF. *Geotail* is on an inbound orbit, crossing the magnetopause near 15 Magnetic Local Time (MLT) and near the magnetic equator. During the period of interest, *Cluster* remains near 19 MLT, at the same low latitudes in the southern magnetic hemisphere. These positions are indicated in Figure 1b. The upstream solar wind conditions for this event are monitored by the Advanced Composition Explorer (ACE), near the L1 Lagrangian point.

[11] This case study shows variations along the flank and under varying IMF clock angle conditions. After careful alignment of the solar wind time series with the observations near the magnetopause in section 2, we estimate the boundary layer thickness and its evolution with time in section 3. In this work, we define a boundary layer where two populations of high- and low-energy electrons are observed simultaneously, which we refer to as the electron boundary layer (EBL). In section 4, we characterize the wave activity at *Cluster*. Section 5 discusses the relations between the degree of wave activity, changes in IMF orientation, latitude and thickness. Section 6 gives a summary of the methodology and results and discusses the potential applicability to data from newly available spacecraft constellations.

2. Magnetosheath Magnetic Field Clock Angle Adjacent to the Magnetopause

[12] A good knowledge of solar wind conditions, which are contemporaneous with observations at the flank is essential for careful correlations between the solar wind properties (e.g., IMF clock angle) and the boundary properties (e.g., wave activity and thickness). We wish to identify a number of periods of relatively constant, but different IMF
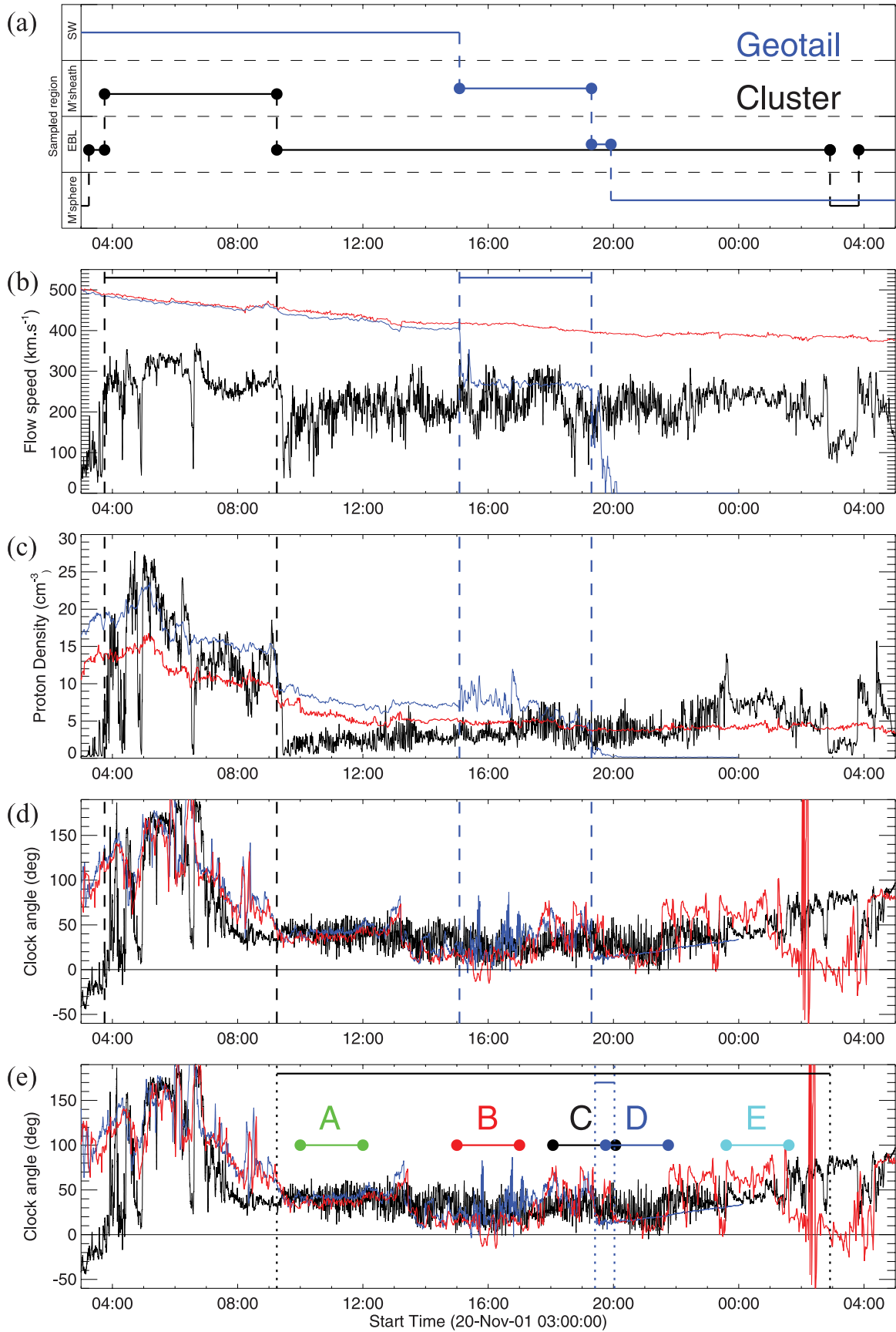
Figure 2

clock angle, over which averages can be assumed reliable for representing conditions near and upstream of *Cluster* along the magnetopause. To this end, we consider plasma transport first in the solar wind and then in the magnetosheath. We choose a 26-hour time interval starting at 3 UT on 20 November 2001. Magnetic and plasma in-situ observations are provided by the instruments listed in Table 1.

[13] We use the High Resolution OMNI (HRO) data product (OMNIWeb Data Documentation, available at http://omniweb.gsfc.nasa.gov/ow_min.html, *King and Papitashvili*, 2005), created at 1 minute resolution to obtain the solar wind conditions. For this event, they are the interplanetary magnetic field and plasma values from ACE, which is located near [228, 40, −12] R_E in the Geocentric Solar Ecliptic (GSE) system. In the HRO product, these values are time-shifted to a model bow shock nose location that varies with changes in solar wind conditions. The solar wind conditions over the 26-hour interval, as observed by ACE, are relatively quiet with intermediate speeds (decreasing steadily from 500 to 380 km s^{-1}) and northward IMF (the components of the IMF in the GSE system are $B_x = -2.0 \pm 1.9$, $B_y = 2.0 \pm 1.9$ and $B_z = 2.2 \pm 2.3$ nT).

[14] Figure 2a indicates schematically the plasma regions sampled by *Geotail* and *Cluster* respectively. *Cluster* reaches apogee near the middle of the interval under study, at 18:01 UT. As the four *Cluster* spacecraft (denoted Ci, $i \in [1, 2, 3, 4]$) with separations of about 2000 km move outward toward apogee, they cross the EBL, between 3 and 4 UT on 20 November, then remain in the magnetosheath for more than 5 hours and cross the magnetopause again, near 09:15 UT, remaining in the EBL for nearly 17 hours. C3 crosses the magnetic equator from the northern to the southern hemisphere at around 07:06 UT on 20 November 2001, while sampling the magnetosheath. *Geotail* is initially in the solar wind and crosses the magnetosheath, from the bow shock to the magnetopause, between 15:05 UT and 19:18 UT. It then crosses the EBL in about 38 minutes and samples the magnetosphere after 19:55 UT.

[15] Figures 2b, 2c, and 2d provide a comparison of the proton bulk flow speeds, proton densities and clock angles between the three data sets from HRO (red), *Geotail* (blue) and *Cluster* C3 (black). The *Geotail* observations during the spacecraft excursion into the solar wind ahead of the bow shock are useful to validate the HRO product. At 15:05 UT, *Geotail* crosses the bow shock at location [14.20, 6.12, 2.15] R_E in the GSE system, duskward of the nose location, predicted to be at [14.48, −0.80, −0.31] R_E (according to the HRO product). Despite a separation distance >6 R_E across the flow direction, Figure 2d shows that inferred values of the IMF clock angle at the bow shock nose are in good agreement with the clock angle measured at *Geotail* in the solar wind.

[16] The magnetosheath flow is inherently more complex to model than in the solar wind, due to various processes [e.g., *Song and Russell*, 2002] that are likely to affect plasma populations and magnetic fields to a greater extent than processes in the solar wind. However, the streamlines near the magnetopause generally originate near the Sun-Earth line. Moreover, as pointed out by *Song et al.* [1992], the clock angle changes little across the bow shock, because of the coplanarity condition. In the approximation of perfect magnetic field draping against the dayside magnetopause [*Fairfield*, 1967; *Crooker et al.*, 1985], the magnetosheath field is tangential to the magnetopause. The preservation of the clock angle is then a fairly good approximation throughout the dayside magnetopause. On the nightside, however, the clock angle is expected to follow the local orientation of the boundary. Therefore the clock angle is expected to be quite well preserved when *Geotail* approaches the dayside magnetopause, but not so well when *Cluster* samples the nightside magnetosheath.

[17] We compute the cross-correlation [*Fuller*, 1995] between the HRO and the *Geotail* clock angle time series. *Geotail* has a sampling resolution of 3 s. The solar wind data set is compared, for different time lags, with overlapping elements from part of the *Geotail* data set, between 17:15 and 19:30 UT, when *Geotail* is closest to the magnetopause (i.e., closest to the streamline originating from the bow shock nose). We compute also the cross-correlation between the HRO and the *Cluster* clock angle time series. In this case, we select the C3 magnetic field time series (with a sampling resolution of 0.2 s) when *Cluster* is in the magnetosheath, between 03:45 and 09:15 UT. In Figures 2 and 3, all time series are 1-min running averages. Figure 3a shows in greater detail the chosen magnetosheath clock angle time series for cross-correlation with the HRO clock angle. To increase the accuracy to which we obtain the time lag returning the highest correlation coefficient, the 1-min cadence solar wind data set is interpolated to the higher magnetosheath resolution time array, while high-frequency perturbations in the magnetosheath are smoothed out in a 1-min running average. The cross-correlation coefficients are shown versus time lags in Figure 3b. The coefficients reach a statistically significant peak (above 0.6 in all cases). Figure 3c shows the alignment between HRO and magnetosheath data sets, after shifting the solar wind time series by the peak correlation time lags. These time lags are 6 min 28 s for *Geotail* and 13 min 20 s for *Cluster*.

[18] Such time lags are consistent with propagation delays due to plasma transport along streamlines from the bow shock nose to the subsolar magnetopause and then along the magnetopause. While this consistency is expected for *Geotail*, it is less clear why it is the case for *Cluster*. Two possible explanations may be given, connected to the large

Figure 2. Overview of conditions sampled by *Geotail* (blue), *Cluster* C3 (black) and inferred at the bow shock from ACE (HRO, in red) over a 26-hour interval starting at 3 UT on 20 November 2001. (a) Plasma environments sampled by *Geotail* and *Cluster*; 1-min running average of (b) proton bulk flow velocities, (c) proton densities, and (d) clock angles; (e) 1-min running average of clock angles after alignment of the *Geotail* and HRO data in the timeframe of the *Cluster* time array. In Figures 2b, 2c, and 2d, vertical dashed lines mark the intervals when either *Cluster* or *Geotail* are observed to be in the magnetosheath. In Figure 2e, vertical dotted lines mark intervals in the boundary layer; five 2-hour time intervals are denoted chronologically from A to E.
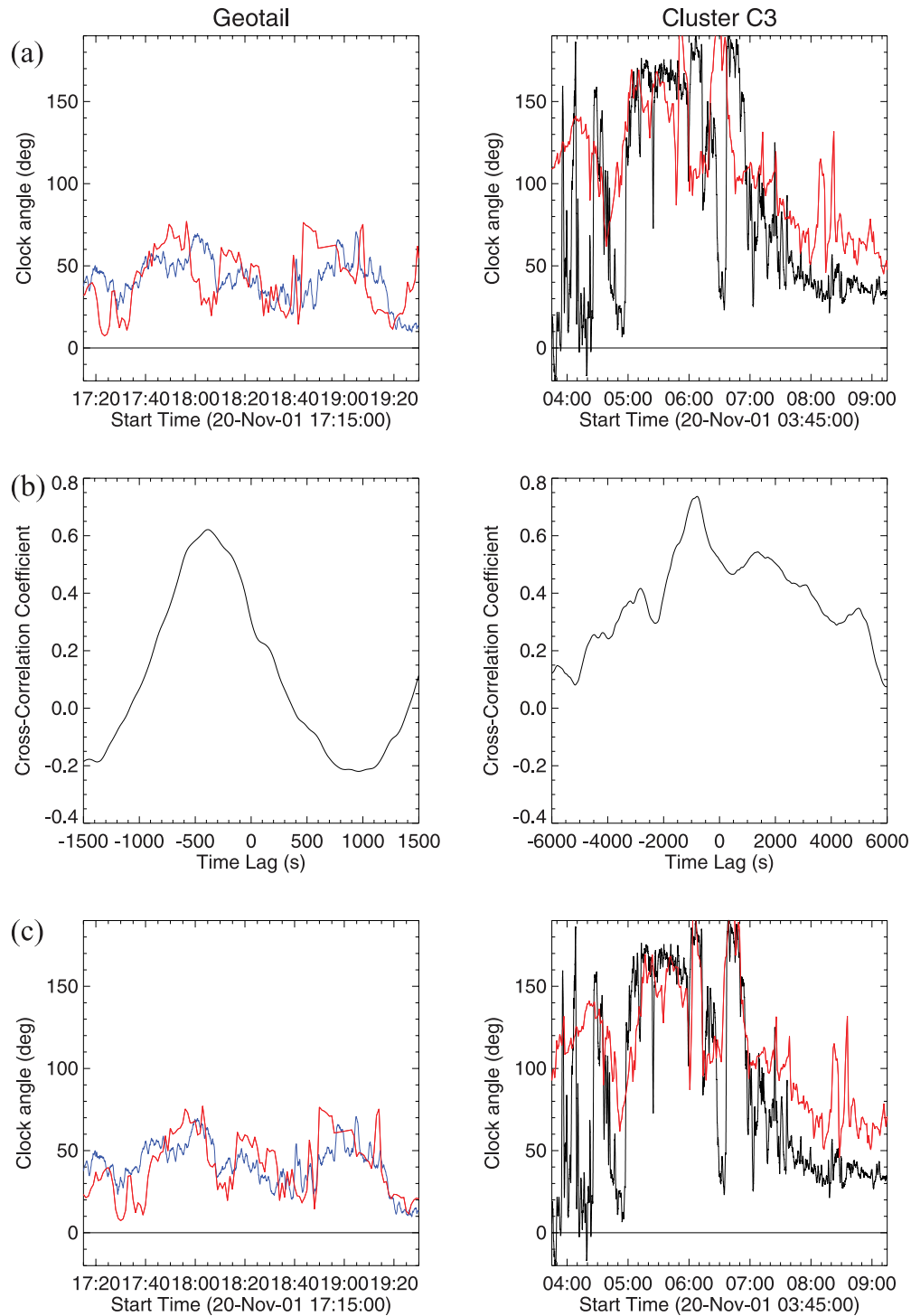
Figure 3. Alignment of magnetosheath magnetic field clock angles from (left) *Geotail* (blue) and (right) *Cluster* C3 (black) with respect to the HRO clock angle (red). (a) Magnetosheath time series chosen for cross-correlation and the original overlapping HRO time series, (b) cross-correlation coefficient versus lag time, and (c) alignment between magnetosheath and HRO time series, after shifting the solar wind data set by the time lag returning the highest cross-correlation coefficient.

and highly variable clock angle in the *Cluster* magnetosheath data set chosen for the cross-correlation (right plots in Figures 3a and 3c). One is that the flaring on the dusk flank offers an oblique magnetopause surface with respect to the noon-midnight meridional plane, which may help to retain, if not the absolute clock angle direction, at least the large variations of the clock angle during the magnetic field draping on that surface. A second explanation is that an IMF

Table 2. Averages (± Standard Deviation) of ACE Solar Wind Proton Bulk Flow Speed, V_{SW}, Proton Density, ρ_{SW}, and IMF Clock Angle, CA, Inferred at the Bow Shock Nose (HRO) and Time Shifted in the Frame of the *Cluster* Spacecraft, for Five 2-Hour Time Intervals on 20 November 2001, Denoted Chronologically From A to E

	Time Interval	V_{SW} (km s^{-1})	ρ_{SW} (cm^{-3})	CA (°)
A	10:00–12:00 UT	443 ± 4	6.0 ± 0.7	36 ± 3
B	15:00–17:00 UT	417 ± 2	4.8 ± 0.2	12 ± 10
C	18:04–20:04 UT	400 ± 5	4.2 ± 0.4	41 ± 18
D	19:45–21:45 UT	390 ± 3	3.8 ± 0.1	19 ± 12
E	23:36–01:36 UT	389 ± 3	4.2 ± 0.3	62 ± 16

field line, which drapes the subsolar point with a large clock angle, say near 90°, will approximately conserve this direction near the equator away from the magnetopause in the magnetosheath, where *Cluster* moves. Therefore variations around that direction are also likely to be retained.

[19] One can argue that, since the streamlines passing the spacecraft, at a few R_E away from the magnetopause in the magnetosheath, do not originate exactly from the bow shock nose, some relatively small variations in the estimated propagation delays can exist. Besides, there must be changes over time in the propagation delay closely related to changes in solar wind speed. However, given the fairly steady solar wind speed over the 26-hour interval and the relatively constant position of *Cluster* along the flank, we do not expect large variations over time in this delay.

[20] From the above analysis, we conclude that, over 22-hour intervals, propagation delays do need to be taken into account for reliable average estimates of solar wind conditions adjacent to the magnetopause, while small variations in the propagation delay do not greatly affect those estimates. We choose five 2-hour time intervals, when *Cluster* is in the EBL, denoted chronologically from A to E, as indicated in Figure 2e. Table 2 gives averages and standard deviations of solar wind conditions (proton bulk flow speed, V_{SW}, proton density, ρ_{SW}, and IMF clock angle) aligned in the frame of the *Cluster* spacecraft for these intervals. The five intervals represent a range of increasing positive clock angles, with values around (B) 12°, (D) 19°, (A) 36°, (C) 41° and (E) 62°, with relatively small variations of the solar wind speed and density between them. Interval D includes the interval studied by *Hasegawa et al.* [2004].

3. Electron Boundary Layer Thickness

[21] We now address the EBL thickness for each of the chosen clock angle intervals. The thickness of a boundary layer is generally characterized using crossings of the layer [e.g., *Mitchell et al.*, 1987]. Complete crossings exist between 3 and 4 UT at *Cluster* and between 19:18 and 19:55 UT at *Geotail*. However, none of the intervals of interest here (A to E) contain a complete crossing by *Cluster* or show a spread of the *Cluster* constellation between the magnetosheath and the magnetosphere. Hence the *Cluster* spacecraft separations of ∼2000 km are not large enough to simultaneously sample both inner and outer edges of the EBL in those time intervals. In this section, we develop a technique to address this issue.

[22] One of the characteristics of the LLBL is the presence of a systematic relationship between the electron number density and the temperature, which may be used as a proxy of satellite's relative position in the LLBL [*Hapgood and Bryant*, 1990, 1992; *Lockwood and Hapgood*, 1997]. In particular, it is possible to define a transition parameter, TP, for a measured data point in the distribution of electron density and temperature.

[23] The new technique follows four main steps, briefly introduced below and described afterward in more details:

[24] Step 1. Evaluation of empirical spacecraft-to-magnetopause model distances (normal to the boundary).

[25] Step 2. Evaluation of the TP time series in complete crossings, notably (a) determination of the log-log function relation, *f*, between electron density and perpendicular temperature and (b) evaluation of the TP range of the EBL.

[26] Step 3. Determination of the form of the correlation, here a linear function, between distances (Step 1) and TP (Step 2) for complete crossings. Together with the TP range of the EBL (Step 2 (b)), this is used to evaluate the EBL thickness.

[27] Step 4. Evaluation of the TP time series for a prolonged interval in the EBL (using the functional form, *f*, found in Step 2 (a)) and low-pass filtering. Derivation of the EBL thickness estimates with time: this is done from a linear fit (function determined in Step 3) between distance time series (Step 1) and smoothed transition parameter time series, ⟨TP⟩, and assuming the TP range of the EBL to be fixed (as determined from Step 2 (b)).

3.1. Step 1

[28] The spacecraft distance to the magnetopause (normal to the boundary) is first estimated from a solar-wind-driven magnetopause model, using the time-varying upstream solar wind conditions as input. Two models are used in this study, the models of *Roelof and Sibeck* [1993] and *Shue et al.* [1997]. The solar wind input parameters are the North-South component of the IMF in the GSM system, B_z, and the solar wind dynamic pressure, P_{SW}. The input conditions are from the HRO 5-min average data product, inferred at the bow shock nose, shifted into the timeframe of the *Geotail* or *Cluster* spacecraft as discussed in section 2. The model outputs are radial distances from the Sun-Earth line to the magnetopause as a function of *X*. The solar wind speed, V_{SW}, is used to correct the magnetopause flaring aberration due to the orbital motion of the Earth. For a given spacecraft position, we find the shortest distance from the spacecraft to the expected magnetopause boundary.

[29] For the given time-varying spacecraft trajectory, we do not expect to obtain very accurate spacecraft-to-magnetopause distances. However we are primarily interested in the changes over relatively short time intervals. In this respect, the imperfections of the models in terms of absolute position of the magnetopause and how well the models predict the observations are not important. For instance, during the 26-hour interval under study, the solar wind flow vector points slightly downward from the Sun-Earth line (around 186.5 ± 2.5° azimuth in the ecliptic plane), with the direction progressively aligning toward the Sun-Earth line as the bulk flow velocity decreases. Corrections to the model outputs using these progressive direction changes
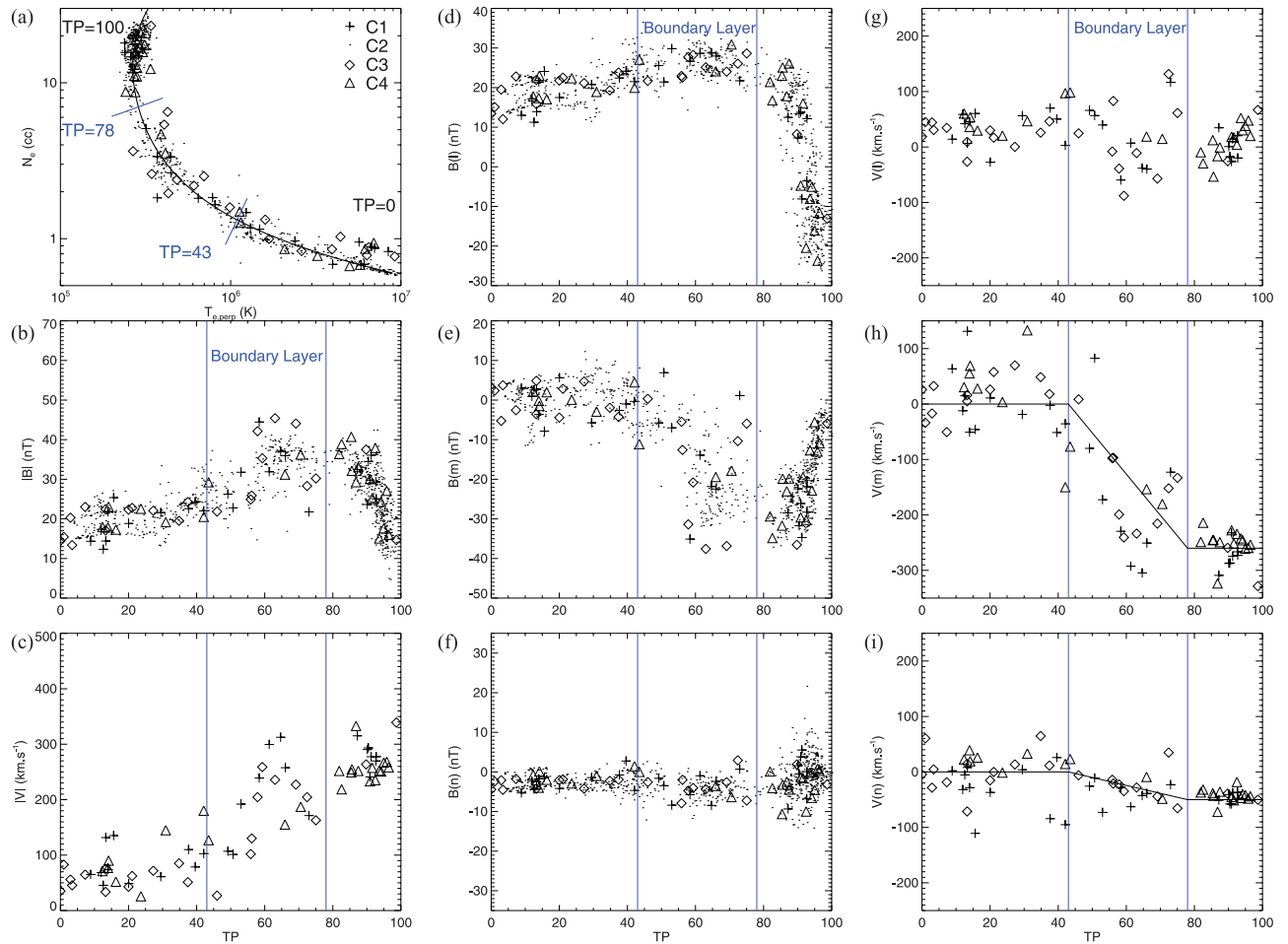
Figure 4. (a) Electron number density versus perpendicular temperature for (crosses) C1, (dots) C2, (diamonds) C3, and (triangles) C4 between 3 and 4 UT on 20 November 2001. The curve fitted to the logarithms of the data points is a polynomial of order 5. The transition parameter, TP, is defined on this curve, between 0 in the magnetosphere and 100 in the magnetosheath. The remaining plots show profiles of intensity and boundary normal components of the magnetic and ion velocity fields reordered versus the TP. Vertical lines indicate the TP interval (43–78) for the EBL. In Figures 4d and 4e, the magnetopause (TP = 78) is characterized by a rotation of the magnetic field. In Figures 4h and 4i, the inner edge of the EBL (TP = 43) coincides with a velocity shear, delineated with piecewise linear profiles for illustration.

over the whole interval will not affect distance changes over short time intervals.

3.2. Step 2

[30] In this step, we characterize the TP range of the EBL under study. *Cluster* electron moments are calculated on the ground from transmitted three-dimensional distributions of electrons with energies between 1 eV and ∼26 keV. The distributions are measured by the two PEACE hemispherical electrostatic analyzers working in the low-energy (LEEA) and high-energy (HEEA) ranges. For the time interval under study the energy ranges are partially overlapping (4.7 eV–2.9 keV for LEEA, 34 eV–26 keV for HEEA). Spacecraft potential corrections are performed using the EFW data set. While C1, C3 and C4 3D data and hence ground moments are available at a time cadence between about 130 and 165 s, C2 moments are available at a cadence of about 4 to 8 s.

[31] Figure 4a shows a log-log plot of the electron number density, N_e, versus perpendicular temperature, $T_{e,\perp}$, for all four *Cluster* spacecraft between 3 and 4 UT on 20 November. The curve fitted to the data points is a polynomial of order 5. TP is a parametric value defined along this curve, normalized between two extreme values: 0 is assigned on the curve to the point nearest to the hottest and most tenuous electron population, observed in the magnetosphere, and 100 is assigned to the point nearest to the coolest and densest population observed in the magnetosheath. Each point in the scatterplot is assigned the value of the closest point on the TP curve. Key field and plasma parameters can then be reordered versus simultaneous measurements of TP. The interpretations based on the TP technique assume a monotonic transition between magnetosheath and magnetospheric plasma across the magnetopause and boundary layer. The remaining plots in Figure 4 show profiles of magnetic and ion velocity fields reordered versus the TP. The ion moments at C1 and C3 are
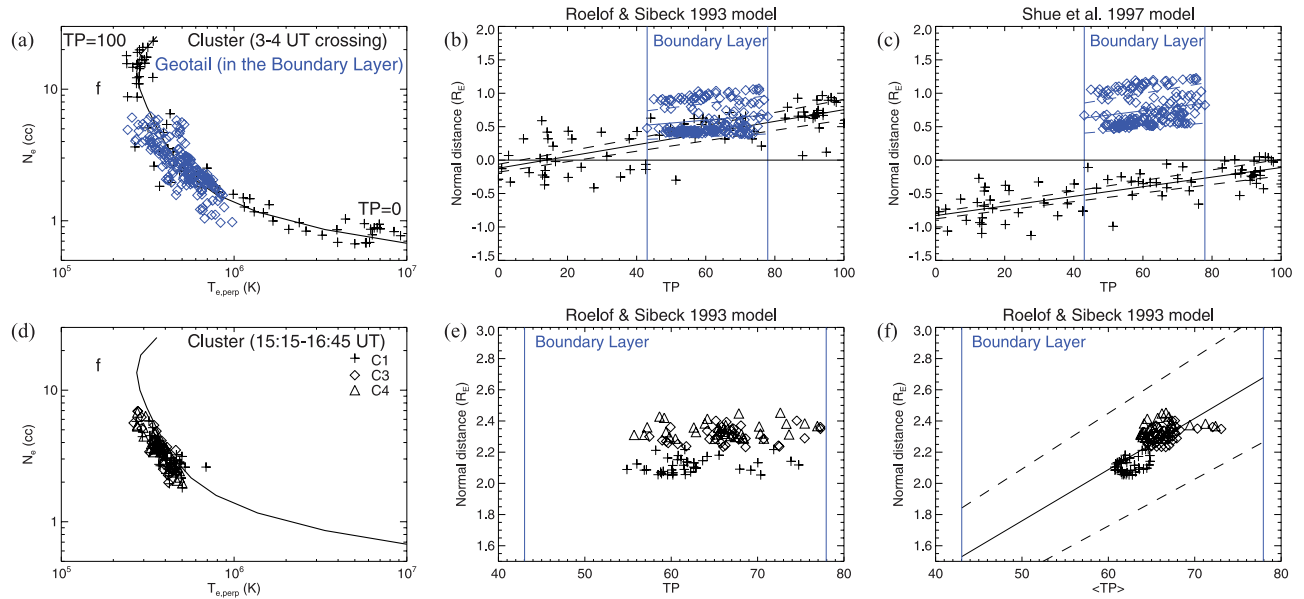
Figure 5. TP fit technique illustrated (upper) across and (lower) inside the boundary layer. (a) Electron number density versus perpendicular temperature for C1, C3, and C4 (black crosses, between 3 and 4 UT) and *Geotail* spacecraft (blue diamonds, in the boundary layer between 19:18 and 19:55 UT). The curve, f, fitted to the logarithms of the data points is a polynomial of order 5. TP is defined on this curve, between 0 in the magnetosphere and 100 in the magnetosheath. (b−c) Normal distance versus TP for each magnetopause model. (d) Electron number density versus perpendicular temperature for (crosses) C1, (diamonds) C3, and (triangles) C4 between 15:15 and 16:45 UT. TP is evaluated using the relation f determined above. (e−f) Normal distance (obtained with the model of *Roelof and Sibeck* [1993]) versus TP and low-pass filtered ⟨TP⟩. The slope, dN/d⟨TP⟩, from a linear fit shown in Figure 5f, is translated into EBL thickness, assuming the TP range for the whole EBL to be constant.

obtained from the CIS Hot Ion Analyzer (HIA) experiment; those at C4 are for protons obtained from the CIS Composition and Distribution Function analyzer (CODIF) experiment. Profiles of magnitudes of the magnetic and velocity fields are shown in the lower left plots of Figure 4, while boundary normal components are shown in the middle and right plots respectively. In the boundary normal coordinate system (**l**, **m**, **n**), **n** is chosen to be the normal to the model magnetopause [*Roelof and Sibeck*, 1993] scaled to the respective spacecraft position in mid-interval (here 03:30 UT), $\mathbf{m} = \mathbf{n} \times \mathbf{z}_{GSM}/|\mathbf{n} \times \mathbf{z}_{GSM}|$ and $\mathbf{l} = \mathbf{m} \times \mathbf{n}$ [*Elphic and Russell*, 1979].

[32] The EBL is characterized by gradually varying profiles in several properties of the magnetic and velocity fields in the LLBL [e.g., *Phan et al.*, 1997]. In this case, we identify the magnetopause with the rotation of the magnetic field at TP = 78 (Figures 4d and 4e) and the inner edge of the EBL with the velocity shear at TP = 43 (Figure 4h). For illustration in Figures 4h and 4i, piecewise linear profiles of the velocity shear layer are delineated for the components V_m and V_n, with average values in the magnetosheath of −260 and −50 km s^{-1} respectively. A few ion data points in the TP profile of V_m display sunward velocities at the inner EBL, consistent with profiles from scatterplots of *Wind* spacecraft crossings in this plasma region [*Phan et al.*, 1997]. Hence we identify the EBL as found between TP = 43 and TP = 78. Populations of high- and low-energy electrons are observed simultaneously in this interval (not shown).

[33] It is of interest to compare the layer crossed by *Cluster* with the one crossed by *Geotail*. Figure 5a shows the electron number density versus perpendicular temperature for C1, C3 and C4 (between 3 and 4 UT) and *Geotail* spacecraft (in the EBL between 19:18 and 19:55 UT). Since, at the time of writing, moments are unavailable for the *Geotail* electron data for this time interval, the data plotted is the proton number density versus a substitute for the electron temperature, $T^*_{e,\perp}$. $T^*_{e,\perp}$ is obtained using the proton temperature at *Geotail* and applying the linear relation between *Cluster* electron and ion temperatures found at C1, C3 and C4 for the same time interval, *viz*

$$T_{e,\perp}[K] = \frac{T_i[K] + 2.34 \times 10^6}{13.9}, \tag{2}$$

where T_i is the proton temperature at *Cluster*. The curve, f, fitted to the logarithms of the data points in Figure 5a is a polynomial of order 5, *viz*

$$f = \log T_{e,\perp} = a_i(\log N_e)^i, \quad i \in [0, 1, 2, 3, 4, 5],$$
$$a_i \in [6.31, -2.90, 5.07, -4.82, 1.98, -0.19], \tag{3}$$

with N_e in cm^{-3} and $T_{e,\perp}$ in K. Equation (3) is close to the function shown in Figure 4a, evaluated without the *Geotail* data points. The TP interval in the boundary layer sampled by *Geotail* agrees with the values found at

Table 3. Boundary Layer Thickness Estimates, ΔL, at *Geotail* and *Cluster* for Different Time Intervals, Given at Midrange (± Half-Range) Between Results Using Empirical Magnetopause Models From *Roelof and Sibeck* [1993] and *Shue et al.* [1997], Respectively[a]

	Time Interval	ΔL (km)	GSM LAT (°)
	Geotail		
(c)	19:18–19:55 UT	1,206 ± 695	1.78 ± 0.02
	Cluster		
		(C1–C3–C4)	(C3)
(c)	03:00–04:00 UT	1,765 ± 361	18.3 ± 0.6
A	10:00–12:00 UT	4,063 ± 1,193	−11.6 ± 0.8
B	15:00–17:00 UT	7,084 ± 863	−11.5 ± 0.6
C	18:04–20:04 UT	5,912 ± 1,687	−8.8 ± 0.3
D	19:45–21:45 UT	7,403 ± 1,589	−8.6 ± 0.2
E	23:36–01:36 UT	7,788 ± 2,455	−15.1 ± 1.8

[a]The average (± standard deviation) of the GSM latitudes is also given. The thickness is derived from a linear fit between transition parameters, TP, and model distances; except for the layer crossings (c), the results of the TP fit technique in 3-min running intervals are time averaged.

Cluster. This supposes a characterization of the TP range of the EBL at widely separated locations and for different time intervals.

3.3. Step 3

[34] We now compare the empirical spacecraft-to-magnetopause distances (evaluated in Step 1) with the TP (evaluated in Step 2) and obtain an estimate of the EBL thickness. Figures 5b and 5c show the spacecraft-to-magnetopause distances, for each model, versus the TP during the two crossings of the boundary layer by *Geotail* and *Cluster.* In each crossing, and for each model, the data points are scattered about a line running from low to high TP with increasing spacecraft-to-magnetopause distance (positive toward the magnetosheath). We obtain linear fits. Hence the slope or conversion parameter (between the TP and spacecraft-to-magnetopause distance) can be used to estimate the EBL thickness for the given TP interval in the EBL. In other words we use this information to calculate an actual physical distance between points of TP = 43 and points of TP = 78.

[35] For the crossing of the boundary layer by *Cluster,* there is a spread in distance in the direction normal to the magnetopause between C3 (most inward), C1 (intermediate) and C4 or C2 (most outward). Therefore the crossings of the inner edge of the EBL and the magnetopause occur at different times but all happen between 3 and 4 UT. To avoid excessive weight of data points from C4 and C2 in the fits, we do not include data from C2, which stands roughly at the same distance as C4 and for which moments with much higher time cadence than the other three spacecraft are available.

[36] A thickness estimate and a standard deviation from the fit are obtained for each of the two empirical magnetopause models, defining a range of extrema. The final thickness estimate given in Table 3 is at midrange (± half-range) between those extrema.

3.4. Step 4

[37] To estimate the variation of EBL thickness with time, we then extend this technique when *Cluster* is sampling the

layer locally, without crossing it, and regard these conversion factors as a proxy for the thickness. In other words, if we know the physical distance between measured points of TP inside the EBL, we can infer the distance between (non-measured) points of TP = 43 and points of TP = 78. The TP is evaluated using the functional form, f (equation (3) found in Step 2). Figure 5d illustrates the scatter of points around this curve, for a 90-min interval (chosen between 15:15 and 16:45 UT). The technique assumes a linear relationship between distance and TP. Therefore, for this method to work in a confined region of the boundary layer, it is critical to have an evenly spread scatter of data points, that can generate a reliable correlation (between distance and TP) and under changing conditions with time.

[38] First, it is critical to have a good spread of spacecraft across the boundary layer. During the prolonged period in the boundary layer, C1 (sampling the inner plasma) and C4 or C2 (sampling the outer plasma) are separated in the normal direction, while C3 is in a relative outward normal motion between the spacecraft, due to the orbital evolution of the *Cluster* tetrahedron. By choosing not to include the C2 data, as in the case of the complete crossing above, we avoid excessive weight of data points toward the outer plasma regions (higher TP) in the linear fits and do not require a separate treatment of the high-cadence C2 data set. Figure 5e is a scatterplot of normal distances versus TP for the example given inside the boundary layer.

[39] Second, we need to eliminate the effect of the wave motions on the TP and higher-frequency TP fluctuations and retain low-frequency variations in the TP time series similar to those in the distances, as expected when controlled by solar wind variations. The result should be a balanced scatterplot, as seen in Figure 5f. Wave motions give large fluctuations on relatively short timescales in TP, as shown in Figure 6a for C1, C3 and C4. These high-frequency perturbations are likely to include perturbations suspected to be caused by KH waves. The empirical spacecraft-to-magnetopause distances, using solar-wind-driven models, are shown for comparison in Figure 6b. In order to reproduce low-frequency variations in the TP time series similar to those in the distances, the high-frequency TP fluctuations are smoothed away in a wavelet à trous decomposition [*Starck and Murtagh*, 2002]. This method decomposes a time series in a sequence of approximations of the signal that have increasing timescales. We sum the approximations with the larger timescales down to a scale, which compares with solar-wind-driven variations. The residual ⟨TP⟩ obtained is shown as a thick red line overlaid on the TP time series in Figure 6a. The wavelet à trous decomposition was found to be better suited than a running average [see also *Foullon et al.*, 2005].

[40] We correlate all residuals ⟨TP⟩ from C1, C3 and C4 in 90-min intervals (running in 3-min steps) with the simultaneous normal distances, N, to the magnetopause and find the slope or conversion factor, $dN/d\langle TP\rangle$, with time (together with the standard deviations from the fits) (see Figure 5f). Those are translated also into EBL thickness, ΔL, assuming the TP interval for the whole EBL to be the constant $\Delta TP = 35$ as for the *Geotail* and *Cluster* crossings (Step 2). The results are shown for both models in Figure 6c. Mid-range values of the thickness and their
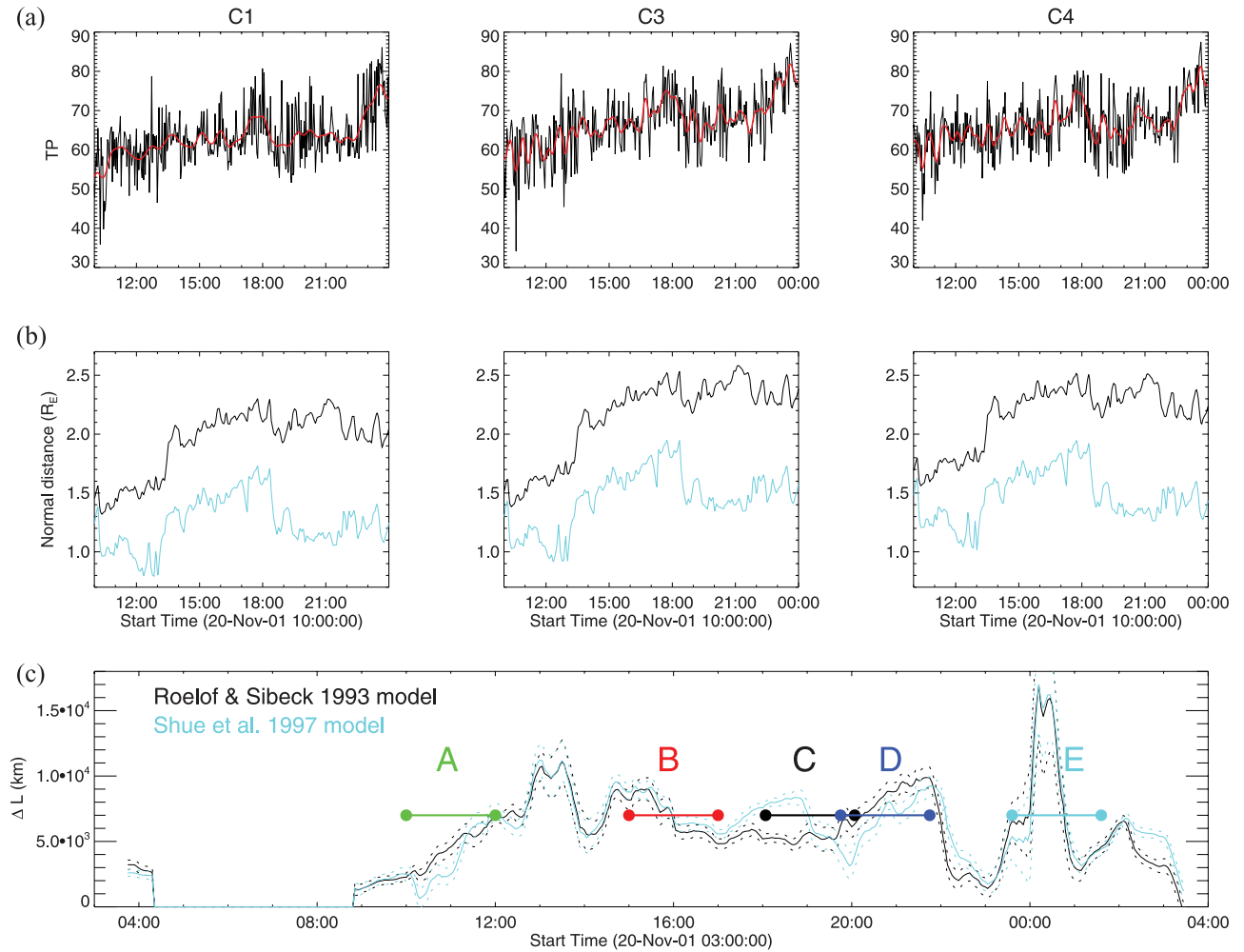
Figure 6. (a–b) Separation of high-frequency fluctuations in transition parameter, TP, due to wave motions inherent to the magnetopause, from larger timescale effects due to solar-wind-driven global motions, for (from left to right) C1, C3, and C4. (a) TP (black) and residual ⟨TP⟩ (red) in a wavelet à trous decomposition. (b) Distance from spacecraft to magnetopause, normal to the magnetopause boundary, obtained with the empirical magnetopause models from *Roelof and Sibeck* [1993] (black) and *Shue et al.* [1997] (cyan). (c) Boundary layer thickness ΔL versus time obtained with C1, C3, and C4, using the empirical magnetopause models; the range of standard deviations is shown with dotted lines; the five time intervals of interest are indicated.

half-ranges are time-averaged for intervals A to E, as given in Table 3.

4. Wave Activity in the Boundary Layer at Cluster

[41] Wave activity may be characterized by phase speeds, wavefront steepness, directions of propagation (defined by the unit $\hat{\mathbf{k}}$-vector), spectral power (which relates to fluctuation amplitudes) and periodicities (which correspond to wavelengths for known phase speeds). We choose data from C2 as reference, because of the higher time cadence of the electron moments obtained with this spacecraft. Figure 7 illustrates the spectral analysis of the wave activity for the interval B with low clock angle ($12 \pm 10°$), between 15 and 17 UT. Figures 7a, 7b, and 7c show the magnetic field time series **B** measured at C2, projected into a boundary normal coordinate system (**l**, **m**, **n**), where **n** is chosen to be the model normal to the magnetopause [*Roelof and Sibeck*, 1993] scaled to the C2 position in mid-interval (here 16:00 UT, see Table 4).

[42] Fluctuation amplitudes in magnetic field are smallest in the direction normal to the magnetopause and are largest in the **m**-direction. We note irregular patterns in the amplitudes and timescales, both in the **l**- and **m**-components, in particular near 15:35 and 16:30 UT, where the fluctuations are smaller. We detrend the time series of the **m**-component, $B(m)$, in a wavelet à trous decomposition, in order to filter out the low frequencies presumably associated with solar-wind-driven variations. The trend indicates an average field of -10.1 nT in the **m**-direction, therefore pointing tailward. With respect to this trend, the variation amplitudes are asymmetric, with the magnetic field intensity variations larger in the sunward direction,
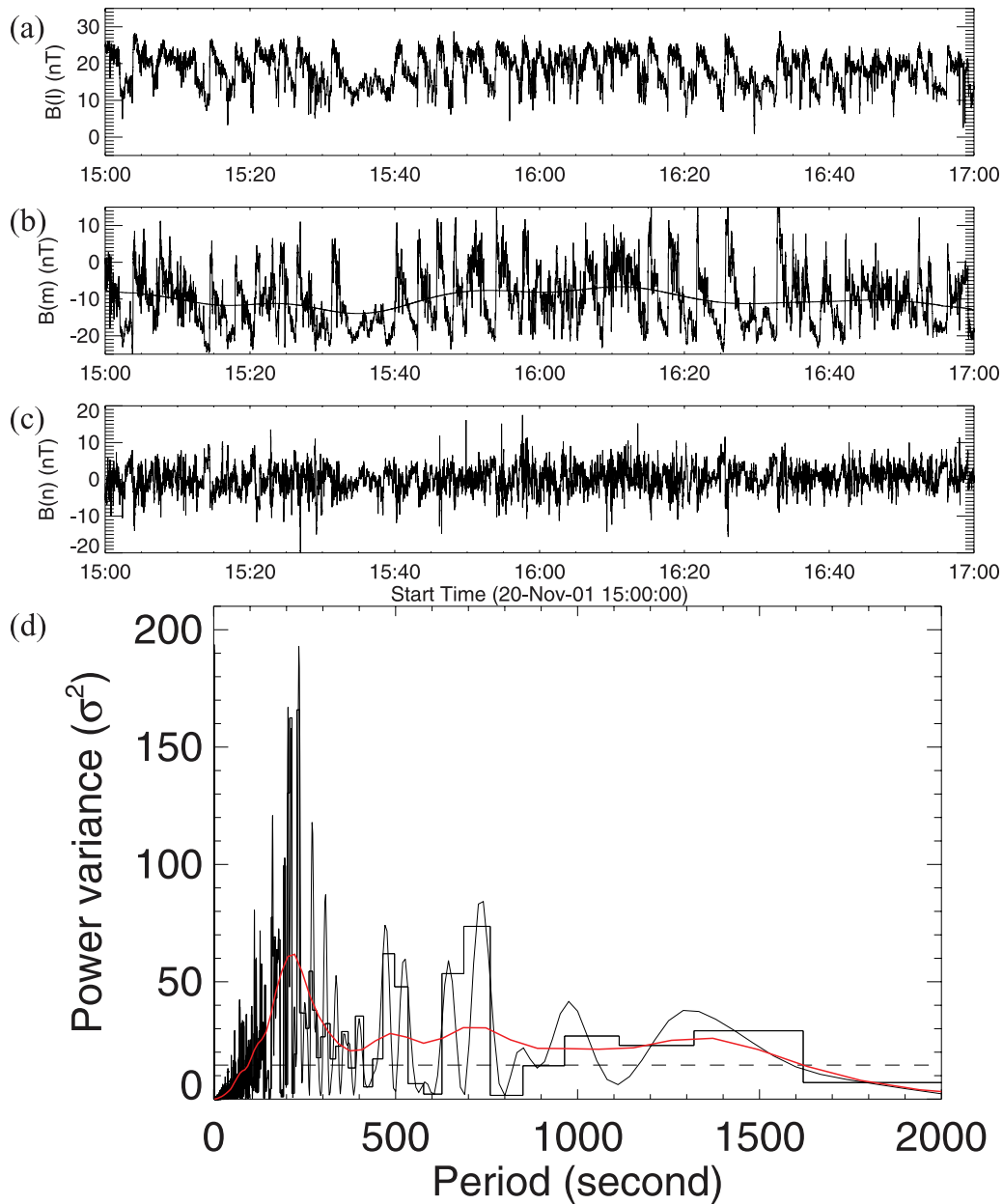
Figure 7. Magnetic wave activity at C2 in the interval B with low clock angle, between 15 and 17 UT on November 20, 2001. (a−c) Magnetic field time series B, projected into a *lmn*-coordinate system; a trend is overlaid on the **m**-component, $B(m)$. (d) Lomb-Scargle periodogram (thin solid), normalized Fourier power spectrum (histogram mode) and normalized global wavelet spectrum (thick red) on the detrended time series $\delta B(m)$. The horizontal dashed line is the 95% confidence level for the periodogram.

reaching up to 30 nT as opposed to 15 nT in the tailward direction. The sunward variations are associated with stronger northward components (in the **l**-direction). In a monotonic boundary layer (with gradual changes of plasma and field quantities, see Figure 4), the magnetic field is observed to rotate between magnetospheric and magnetosheath values. The tailward trend is consistent both with a dipole field stretched tailward in the southern hemisphere and for an IMF with a negative B_x component. Figure 8 illustrates one particular oscillatory structure, observed between 15:39 and 15:43 UT by all four *Cluster* spacecraft. Shown in Figure 8a are the respective components

$B(m)$ of the magnetic field and in Figure 8b the electron perpendicular temperature $T_{e,\perp}$ calculated onboard the PEACE instruments. In a monotonic boundary layer, a temperature decrease/increase indicates an inward/outward motion (toward/away from the magnetosphere). The inward motion, resulting in a sampling of the outer boundary layer, is here associated with the sunward turning of the magnetic field direction, itself concomitant with the northward turning (Figures 7a and 7b). The association of the temperature decrease and the stronger northward magnetic field direction indicates that the magnetic field in this particular location is reminiscent of the magnetosheath field.

Table 4. Wave Activity in the Boundary Layer at *Cluster* for Five Time Intervals on 20 November 2001: Details of Four-Spacecraft Timing Analysis[a]

Interval	A (10–12 UT)	B (15–17 UT)	C (18:04–20:04 UT)	D (19:45–21:45 UT)	E (23:36–01:36 UT)
		Boundary Normal Coordinates (GSM)			
l	[0.074, 0.138, 0.988]	[0.078, 0.136, 0.988]	[0.061, 0.104, 0.993]	[0.064, 0.106, 0.992]	[0.109, 0.171, 0.979]
m	[0.882, −0.471, 0.000]	[0.869, −0.495, 0.000]	[0.862, −0.507, 0.000]	[0.855, −0.518, 0.000]	[0.843, −0.538, 0.000]
n	[0.465, 0.871, −0.156]	[0.489, 0.858, −0.157]	[0.504, 0.855, −0.120]	[0.514, 0.848, −0.124]	[0.527, 0.826, −0.203]
		Four-Spacecraft Timings From B(m) Time Series			
a) Center	10:51:55:765 UT	15:40:23:301 UT		20:21:24:235 UT	00:21:46:765 UT
Ci (s)	[14.3,−14.3,6.1,0.3]	[13.4,−13.4,−5.3,−0.2]		[11.5,−11.5,6.1,7.1]	[22.2,−4.8,−22.2,9.8]
b) Center	10:52:54:292 UT	15:41:03:051 UT		20:19:37:635 UT	
Ci (s)	[−16.0,−7.6,−10.6,16.0]	[−17.0,−3.3,17.0,13.6]		[−12.7,0.3,9.1,12.7]	
		Four-Spacecraft Timings From $T_{e,\perp}$ Time Series			
a) Center	10:51:40:711 UT	15:40:11:880 UT	19:03:25:122 UT	20:21:30:676 UT	
Ci (s)	[5.7,−5.7,4.9,−1.1]	[11.7,−11.7,−2.1,5.1]	[13.8,−13.8,−2.7,4.8]	[11.3,−11.3,−7.2,2.7]	
b) Center	10:55:45:819 UT	15:41:43:609 UT	19:02:43:308 UT	20:19:39:754 UT	23:44:31:636 UT
Ci (s)	[−22.1,3.8,2.3,22.1]	[−15.6,4.8,9.6,15.6]	[−12.7,−6.0,12.7,9.3]	[−10.0,−0.5,10.0,7.2]	[−27.7,5.7,27.7,20.3]
		Wavefront Directions (GSM)			
$\hat{\mathbf{k}}_{B,a}$	[−0.639, −0.767, −0.0516]	[−0.702, −0.698, 0.140]	-	[−0.838, −0.532, −0.119]	[−0.598, −0.719, 0.354]
$\hat{\mathbf{k}}_{T,a}$	[−0.406, −0.904, −0.133]	[−0.854, −0.520, −0.025]	[−0.788, −0.589, −0.180]	[−0.759, −0.651, −0.014]	-
$\hat{\mathbf{k}}_a$	[−0.522, −0.836, −0.092]	[−0.778, −0.609, 0.057]	[−0.788, −0.589, −0.180]	[−0.798, −0.592, −0.066]	[−0.598, −0.719, 0.354]
$\hat{\mathbf{k}}_{B,b}$	[−0.390, 0.738, −0.5502]	[0.023, 0.635, −0.772]	-	[−0.145, 0.975, −0.168]	-
$\hat{\mathbf{k}}_{T,b}$	[−0.000, 0.790, −0.613]	[0.049, 0.873, −0.485]	[−0.154, 0.798, −0.583]	[−0.019, 0.929, −0.370]	[0.121, 0.992, −0.031]
$\hat{\mathbf{k}}_b$	[−0.196, 0.764, −0.582]	[0.036, 0.754, −0.628]	[−0.154, 0.798, −0.583]	[−0.082,0.952,−0.269]	[0.121, 0.992, −0.031]
		Velocities (km s^{-1})			
$V_{B,a}$	67.45	71.18	-	109.73	44.48
$V_{T,a}$	151.28	83.10	70.60	80.61	-
$V_{k,a}$	109.36 ± 41.92	77.14 ± 5.96	70.60	95.17 ± 14.56	44.48
$V_{B,b}$	57.30	46.02	-	66.89	-
$V_{T,b}$	44.34	52.03	65.16	85.29	36.29
$V_{k,b}$	50.82 ± 6.48	49.03 ± 3.00	65.16	76.09 ± 9.20	36.2894

[a]Boundary normal coordinates (**l**, **m**, **n**) at mid-interval and at the C2 location; Timings of magnetospheric exit motions, *a*, and entry motions, *b*, on selected oscillatory structures (at Ci, $i \in [1, 2, 3, 4]$, relative to center); directions $\hat{\mathbf{k}}$ and speeds V of wave fronts determined from four-spacecraft timing analysis on those oscillatory structures. Subscripts B and T refer to the magnetic field and temperature data sets respectively.

[43] A global (time-averaged) Morlet wavelet power spectrum of the detrended time series $\delta B(m)$ is shown in Figure 7d. The global wavelet spectrum is normalized (with the squared wavelet variance σ^2) and compared to the normalized Fourier power spectrum. The global wavelet spectrum gives a smoothed version of the power spectrum [*Torrence and Compo*, 1998]. A higher frequency resolution is achieved by computing the Lomb-Scargle periodogram [*Horne and Baliunas*, 1986; *Scargle*, 1982; *Foullon et al.*, 2004]. The 95% confidence level for the periodogram was computed according to *Bai and Cliver* [1990]. The power spreads above the confidence level into three distinct groups of periodicities. The highest peaks in the periodogram cluster around a dominant period of (1) 222 s (4.50 mHz). This period is consistent with the size of individual oscillatory structures, whose amplitudes dominate in the time series when inspected visually. Lower peaks can be distinguished at larger periods near (2) 485 s (2.06 mHz) and (3) 686 s (1.46 mHz). All these periods are in the Pc5 range.

[44] To interpret these periods in terms of length scales or wavelengths, we perform four-spacecraft timing analysis [*Russell et al.*, 1983; *Schwartz*, 1998] on the boundaries of oscillatory structures in the time series $B(m)$ and $T_{e,\perp}$. This method assumes a wavefront to be close to planar and to move with constant velocity on the scale size of the spacecraft separation. The observation times of the wavefront at each four spacecraft can then be used to calculate the speed of the front motion, V_u, and direction of motion given by the $\hat{\mathbf{u}}$-vector. The method consists in solving the 3×3 system of equations describing the relation $\mathbf{r_{ij}} \cdot \hat{\mathbf{u}} = t_{ij}V_u\hat{\mathbf{u}}$ in a Cartesian system for three pairs of spacecraft, C_i and C_j ($i \neq j$), where $\mathbf{r_{ij}}$ is the separation vector between any spacecraft pair and t_{ij} is the time difference for the wavefront to pass between this pair.

[45] The times of the wavefront passages are determined at each spacecraft for a particular oscillatory structure, as shown by filled circles in Figures 8a and 8b. The timings are determined in a consistent manner either semi-automatically in the time series $B(m)$ or manually in the time series $T_{e,\perp}$. Since the magnetic field in the boundary layer may be highly perturbed, the semi-automated method is designed with a multi-scale approach: it consists of taking local extrema in the time derivative of wavelet à trous residuals $\langle B(m) \rangle$ that are recurring for different scales or levels of smoothing. The timings obtained are checked by visual inspection afterward and any missing timing is selected manually. The timings in the temperature time series, which have a lower spin time-resolution of 4 s, are chosen at mid-value in the steepest temperature jumps across the 4 spacecraft [see also *Owen et al.*, 2004].

[46] Furthermore, the electron perpendicular temperature, $T_{e,\perp}$, is used to identify the direction of the motion with
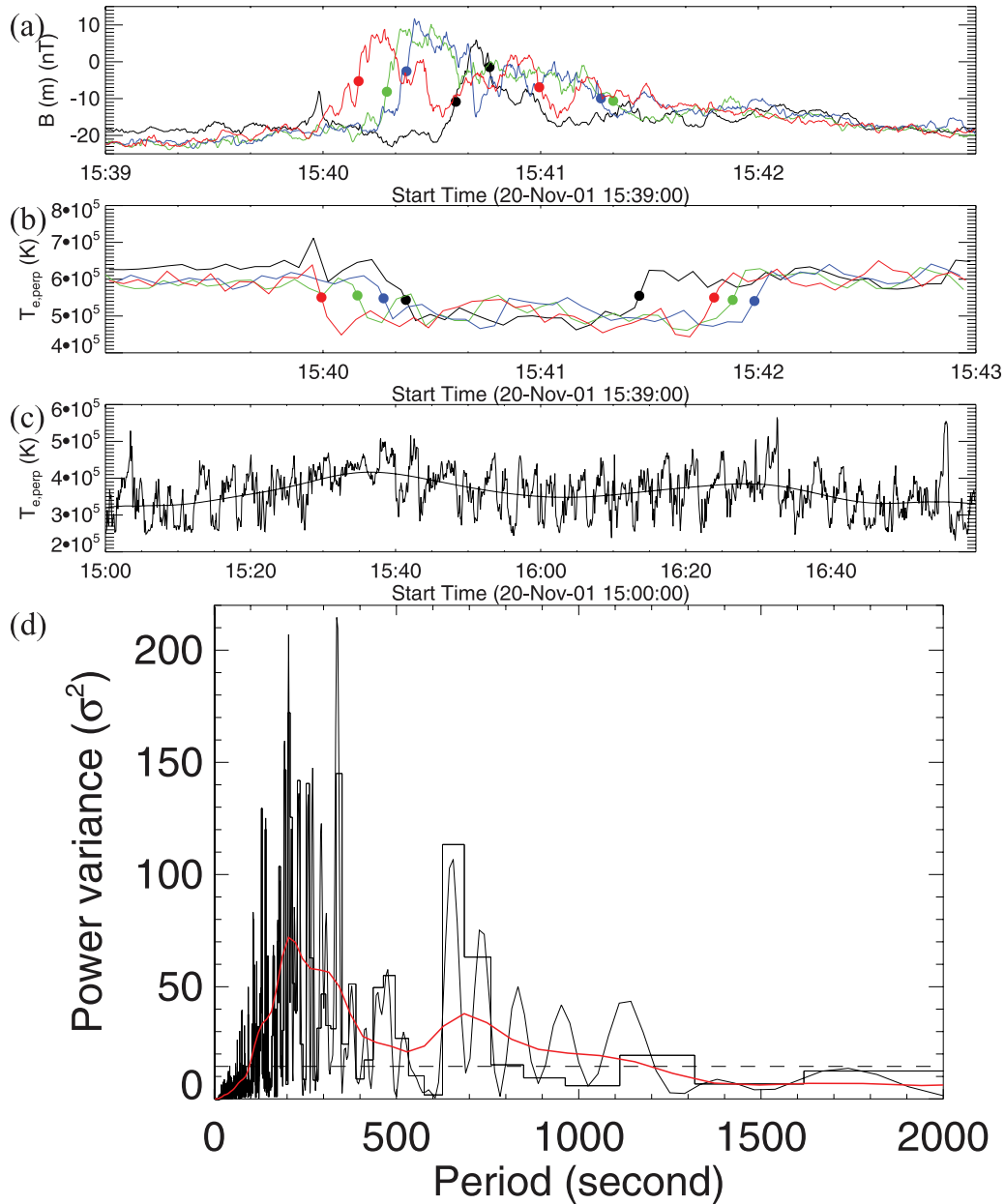
Figure 8. Wave activity characterization from the magnetic field time series and from electron temperature data in the interval B with low clock angle, between 15 and 17 UT on November 20, 2001. (a) Components $B(m)$ of the magnetic field and (b) electron perpendicular temperature $T_{e,\perp}$ from onboard PEACE moments at (black) C1, (red) C2, (green) C3, and (blue) C4, showing one oscillatory structure and the timings, indicated as filled circles, chosen for four-spacecraft timing analysis; temperature decreases and increases indicate inward and outward motions, respectively (toward and away from the magnetosphere). (c) Electron perpendicular temperature $T_{e,\perp}$ from the high-resolution calibrated data set at C2 with a trend overlaid. (d) Lomb-Scargle periodogram (thin solid), normalized Fourier power spectrum (histogram mode) and normalized global wavelet spectrum (thick red) on the detrended time series $\delta T_{e,\perp}$. The horizontal dashed line is the 95% confidence level for the periodogram.

respect to the magnetosphere. A decrease or an increase in temperature is taken to indicate inward or outward motions of the boundary front (toward or away from the magnetosphere). For the oscillatory structure representing period B, the average speeds obtained with magnetic and plasma time series are $V_{k,a} = 77 \pm 6$ km s^{-1} for inward and $V_{k,b} = 49 \pm 3$ km s^{-1} for outward motions, along directions denoted $\hat{\mathbf{k}}_{\mathbf{a}}$ and $\hat{\mathbf{k}}_{\mathbf{b}}$ respectively (see Table 4 for details). The average

phase speed, $V_{k,lm}$, between pairs of motions and projected on the lm-plane is

$$V_{k,lm} = \left(\frac{V_{k,a} + V_{k,b}}{2} \right) \frac{\sqrt{\bar{k}_l^2 + \bar{k}_m^2}}{|\bar{k}|} \text{ , with } \bar{\mathbf{k}} = \frac{\hat{\mathbf{k}}_{\mathbf{a}} + \hat{\mathbf{k}}_{\mathbf{b}}}{2}. \quad (4)$$

For the structure representing period B, $V_{k,lm} = 62 \pm 14$ km s^{-1}.

Table 5. Wave Activity in the Boundary Layer at *Cluster* for Five Time Intervals on 20 November 2001: Summary of Results[a]

Interval	A (10–12 UT)	B (15–17 UT)	C (18:04–20:04 UT)	D (19:45–21:45 UT)	E (23:36–01:36 UT)
			Direction Angles (°)		
$\phi_{k,a}$	86.0	67.7	66.6	67.4	83.1
$\phi_{k,b}$	−51.3	−65.8	−51.4	−54.8	−64.1
θ_{k_a}	−14.3	−5.0	−16.7	−10.4	9.1
θ_{k_b}	−29.6	−31.6	−30.3	−10.0	8.7
θ_k	−21.9 ± 7.6	−18.3 ± 13.3	−23.5 ± 6.8	−10.2 ± 0.2	8.9 ± 0.2
			Phase Speeds (km s^{-1})		
V_k	80 ± 29	63 ± 14	68 ± 3	86 ± 9	40 ± 4
$V_{k,lm}$	76 ± 28	62 ± 14	67 ± 3	85 ± 9	40 ± 4
			Periods (s)		
(i)	179 ± 8	213 ± 9	187 ± 0 (301 ± 13)	215 ± 28	232 ± 10
(ii)	465 ± 20	430 ± 56	451 ± 77	487 ± 42	553 ± 24
(iii)	985 ± 169	686 ± 0	722 ± 93	828 ± 142	629 ± 0
			Wavelengths λ (km)		
(i)	13,801 ± 5,236	13,216 ± 3,113	12,529 ± 561 (20,167 ± 942)	18,254 ± 2,609	9,298 ± 970
(ii)	35,797 ± 13,581	26,630 ± 6,790	30,248 ± 5,422	41,381 ± 4,760	22,114 ± 2,307
(iii)	75,817 ± 32,300	42,527 ± 9,603	48,397 ± 6,535	70,378 ± 13,354	25,160 ± 2,516
			$k\Delta L = 2\pi\Delta L/\lambda$		
(i)	1.85 ± 1.13	3.37 ± 1.04	2.96 ± 0.89 (1.84 ± 0.55)	2.55 ± 0.64	5.26 ± 1.85
(ii)	0.71 ± 0.44	1.67 ± 0.57	1.23 ± 0.43	1.12 ± 0.27	2.21 ± 0.78
(iii)	0.34 ± 0.25	1.05 ± 0.30	0.77 ± 0.25	0.66 ± 0.18	1.94 ± 0.68

[a]Direction angles (ϕ_k, θ_k) and speeds V_k of wavefronts determined from four spacecraft timing analysis (subscripts *a* and *b* refer to magnetospheric exit motions and entry motions *b*, respectively, no subscript indicates the average for the two fronts); periods from power spectra, averaged between dominant periods in magnetic field time series $\delta B(m)$ and temperature variations $\delta T_{e,\perp}$ at C2 in the range (i) 4–10 mHz, (ii) 1.6–2.9 mHz, and (iii) below 1.6 mHz; the corresponding wavelengths (on the *lm*-plane); the corresponding wave number-thickness combinations.

[47] We also characterize motion directions with two direction angles of a $\hat{\mathbf{u}}$-vector in a spherical projection of the ($\mathbf{l}$, $\mathbf{m}$, $\mathbf{n}$) system. These direction angles are respectively

$$\phi_u = \arctan\left(\frac{u_n}{u_m}\right) + 2\pi, \qquad (5)$$

an angle characterizing the wavefront steepness in the *mn*-plane, with $\phi_u = 0$ indicating a front normal pointing in the $-\mathbf{m}$-direction (i.e., tailward) and ϕ_u positive toward the magnetosphere, and

$$\theta_u = \frac{\pi}{2} - \arccos\left(\frac{u_l}{|u|}\right), \qquad (6)$$

an elevation angle characterizing the North-South deviation of the $\hat{\mathbf{u}}$-vector from the *mn*-plane (positive from South to North). For the directions $\hat{\mathbf{k}}_\mathbf{a}$ and $\hat{\mathbf{k}}_\mathbf{b}$ in period B, $\phi_{k,a} = 68°$, $\phi_{k,b} = -66°$ and the average of the elevation angles ($\theta_{k,a}$ and $\theta_{k,b}$) is $\theta_k = -18 ± 13°$. The angles ϕ_k are consistent with an oscillatory wave travelling tailward and the angle θ_k indicates a wave travelling with a southward component.

[48] Finally, to confirm the dominant periods and give error estimates, we take the power spectra of the temperature variations, $\delta T_{e,\perp}$, as illustrated in Figures 8c and 8d. We find similar peaks near (1) 204 s (4.90 mHz), (2) 374 s (2.67 mHz), and (3) 686 s (1.46 mHz). Therefore the dominant periods, averaged between the two spectra, are (1) 213 ± 9 s, (2) 430 ± 56 s, and (3) 686 s. Multiplying the average phase speed $V_{k,lm}$ with each dominant period, we

obtain corresponding wavelengths, λ, of the order of 2.1 ± 0.5, 4.2 ± 1.1 and 6.7 ± 1.5 R$_\mathrm{E}$.

[49] These three ranges of wavelengths, obtained in an unconventional fashion by combining results from four-spacecraft timing and spectral analysis, may indicate multi-scale structures. Results for each of the five clock angle intervals are presented in Table 5 (with details of four-spacecraft timing analysis given in Table 4). Periods from power spectra are averaged between dominant periods in magnetic field time series $\delta B(m)$ and temperature variations $\delta T_{e,\perp}$ at C2 in the range (1) 100–250 s (4–10 mHz), (2) 345–625 s (1.6–2.9 mHz) and (3) above 625 s (below 1.6 mHz). A secondary periodicity (i), found during interval C, is indicated between brackets. For the dominant oscillatory structure (i), during interval D, we note that we obtain wavelength estimates of 2.5–3.3 R$_\mathrm{E}$ (based on the phase speed from four-spacecraft timing), as opposed to the 6.3–8.6 R$_\mathrm{E}$ estimate given by *Hasegawa et al.* [2004] (based on ion velocity measurements).

5. Results and Discussion

5.1. Local Versus Remote Production

[50] At a given point on the flank magnetopause, tailward of the terminator, several types of wave activity may be present: locally and remotely generated waves from the convectively unstable KH surface mode, waves from other KH modes and other possible effects. Locally generated waves originate from a source region close to the observer. Remotely generated waves originate from a source region toward the dayside. For our discussion, all other waves and motion effects can be neglected.

[51] We first discuss whether wave activity may be explained by *local production*, for which instability conditions are satisfied with local input values defining the initial states and linear theory is then applicable. Simulations of the KH instability, which include a finite LLBL thickness [e.g., *Walker*, 1981; *Miura and Pritchett*, 1982], lead to results in which the thickness controls the growth rate (i.e., wave amplitude). Instability and the maximum growth rate occur for preferred combinations $k\Delta L$. This property is valid at the magnetopause, but also at the inner edge of the boundary layer. Wave modes of the magnetopause and inner edge are decoupled for wavelengths smaller than ΔL. Instability regions at the inner edge, where the magnetic field shear is usually minimal, are broader than at the magnetopause. Yet the growth rates are smaller (presumably due to the lower velocity shear), and so in general we expect less activity on the inner edge than on the adjacent magnetopause [F98].

[52] The wavelengths in Table 5 are generally longer than the EBL thickness estimates (Table 3). In such cases and provided that elements of the EBL satisfy the required model representations, theory predicts a coupling between wave modes of the magnetopause and inner edge of the boundary layer. Ideal linear MHD compressible simulations for a set of representative local conditions across the magnetopause for this event have been performed and reported by *Gnavi et al.* [2006]. Their input parameters are estimated for the period between 14 and 17 UT, covering interval B. These are given to be $B_1 = B_2 = 20$ nT, $V_1 = 300$ km s^{-1}, $V_2 = 0$ km s^{-1}, angles $(\mathbf{B}_1, \mathbf{V}) = 80°$, $(\mathbf{B}_2, \mathbf{V}) = 30°$, with $\mathbf{V} = \mathbf{V}_1 - \mathbf{V}_2 (= \mathbf{V}_1)$, $n_1 = 10$ cm^{-3}, $n_2 = 1$ cm^{-3}, plasma temperatures $T_1 = 3.5$ MK (0.3 keV) and $T_2 = 23.2$ MK (2 keV), where indices 1 and 2 refer respectively to the magnetosheath and magnetospheric environments, on both sides of the boundary layer. Although they are difficult to check in this period (when *Cluster* is inside the layer), the given values are roughly consistent with TP profiles for the earlier crossing between 3 and 4 UT (Figure 4) and the extrema reached by the proton density time series before and after entering the EBL near 9:15 UT (Figure 2d). The simulation results indicate that instability is more likely to occur for the combination $k\Delta L \sim 0.25$ and maximum growth rate for $k\Delta L \sim 0.35$. Table 5 shows that such conditions are not generally met at *Cluster* except for perturbations (ii) and (iii) in interval A.

[53] Furthermore, the observations in section 4 indicate that, as the motions are directed inward, *Cluster* C2 samples the outer boundary layer where the reminiscent magnetosheath field is pointing sunward, as opposed to the IMF in the solar wind pointing tailward (with negative B_x component). For surface waves with lower phase speeds than the outer magnetosheath speed, this can be interpreted as the result of bending of field lines whereby the magnetosheath field is caught up and dragged sunward by the surface waves. Such bending of field lines is expected to have a strong stabilizing effect on the local onset of the KH instability.

[54] Thus, the observed waves, most importantly the ones in the (i) range, are unlikely to be locally generated by the KH mechanism. They possess, however, characteristic KH behavior, in their wavefront steepness and propagation direction, which attests to their remote origin. The KH surface mode is convectively unstable away from the stagnation region and the associated disturbances are expected to grow very quickly as they convect tailward around the magnetosphere, so that nonlinear effects may dominate. In this event, in particular, speeds and directions differ systematically between inward and outward motions. The steepness angles ϕ_k indicate wavefronts travelling tailward with the leading edges (with outward motions) generally steeper than the trailing edges (with inward motions), a geometry similar to the wave morphology found in events analyzed by *Fairfield et al.* [2000] and *Owen et al.* [2004]. Correspondingly, the speeds are generally faster for inward motions (as shown in Table 4), which confirm them as projections of the phase speed along the boundary normals. This is qualitatively consistent with waves in their growing phase, hence of remote origin.

5.2. Changes in Electron Boundary Layer Thickness

[55] The evaluation of the EBL thickness in section 3 assumes a monotonic transition between magnetosheath and magnetospheric plasma, generally required to apply the TP technique. In the presence of waves or vortices, this supposes that the oscillatory or rolled-up plasma conserves its gradual density and temperature properties in TP-space. We also assume that a fixed TP range of the EBL can be used at widely separated locations and in different time intervals. For our purpose, the properties of interest are the smoothed TP values, devoid of waves or vortices. By correlating the residuals $\langle TP \rangle$ with spacecraft-to-magnetopause model distances, we extract the macroscopic information in the data. Multiple spacecraft, spread across the boundary layer, are critical for obtaining correlation factors with a reasonable time cadence. We recognize that empirical solar-wind-driven models have limitations. Although accuracy in the distances is not essential, since we are interested in their variations, the use of two magnetopause models, rather than just one, warrants reliable estimates. The changes in correlation factors obtained, corresponding to changes in thickness of the EBL, are therefore likely to represent signatures of a plasma transport evolution, with time and space.

[56] The LLBL broadening and the mixing of plasma in the LLBL may be separate or connected phenomena contributing to the overall formation of the LLBL. When all spacecraft near the dusk magnetopause are sampling the EBL simultaneously, in interval C, we infer that the layer is five times thicker at *Cluster* than at *Geotail*. This result confirms the broadening of the layer with distance along the flank, obtained statistically by *Mitchell et al.* [1987]. An increase in thickness of the LLBL with distance from the subsolar point might be expected based on the gas-dynamic behavior of a classical boundary layer that forms by viscous interaction at a stationary interface between gas flowing parallel to the interface [e.g., *Antonova*, 2005]. However, together with Table 2, Table 3 indicates variations in EBL thickness, temporal or spatial, that may depend on IMF clock angle and geomagnetic latitude.

[57] To investigate further the possible role of waves in the widening of the electron LLBL, we next discuss these parameters in relation with the degree of wave activity at *Cluster*. Note also that when *Geotail* crosses the boundary layer during the time interval C, with relatively large clock

angle, the position of *Geotail* near the equator and close to the stagnation region (Figure 1) is not the most favorable for meaningful comparison with the wave activity at *Cluster*. Moreover, to derive properties, including the phase speed, of wave activity at *Geotail*, would require a single spacecraft method as employed by *Lepping and Burlaga* [1979], which assumes a sinusoidal shape of the waves. For these reasons, we leave out the comparison between the two-point observations at *Cluster* and *Geotail* during the time interval C.

5.3. Predicted Signatures of KH Remote Production in the Parameter Space

[58] Several factors may affect wave behavior: the changing (equilibrium) conditions of the medium in which the waves propagate, but also factors related to the nonlinear evolution of the waves. For instance, as reported in our observations, the thickness of the boundary layer may vary locally (independently of the presence of perturbations). This is expected to affect KH activity of local as well as remote origin. In principle, the sum of all types of activity observed on the flank magnetopause may be non-linear (through interaction, coalescence or merging of vortices for instance). However, wave activity of remote origin, if present, is likely to dominate, with the largest wavelengths and amplitudes, over other types of wave activity (section 1).

[59] As the GSM clock angle tends to zero, part of the dayside magnetopause becomes KH unstable with larger source regions [F98, Figure 1] and with higher growth rates [*Miura*, 1995, F98]. Then the KH waves propagate down the tail and are likely to reach a nonlinear stage. At a location downstream of this source region (near the equator in the case of low clock angle), the detected wave activity corresponds to remote production. We pose a first hypothesis, namely that the non-linear stage for the associated remotely generated waves is likely to be reached at a more downstream position along the magnetospheric boundary for larger clock angle, because of the drift of the source regions toward the tail and the lower growth rates. Another hypothesis proposed by F98, which does not necessarily require nonlinear growth, is that the longest wavelengths are controlled by the dimensions of the source regions in the direction of the wave vector **k** along the magnetopause surface (i.e., the lateral extent of the unstable regions in a direction predominantly perpendicular to the interplanetary and geo-magnetic fields, so as to minimize the right-hand side of equation (1)). Therefore, as the clock angle tends to zero, we expect at the flank to observe longer wavelengths and larger amplitudes. We pose the hypothesis that, if remote production is present, changes in clock angle will affect more strongly the waves of remote origin, whether they coexist or not with waves of local origin.

[60] Moreover, the orientation of a $\hat{\mathbf{k}}$-vector, as observed downstream of the source region in a favorable location, may be considered to point in a direction, which, to a first approximation, retains the signature of the magnetic topology of the upstream source region, i.e., in a direction predominantly perpendicular to the interplanetary and geomagnetic fields. As such, the $\hat{\mathbf{k}}$-vector orientation may be regarded as important to indicate the origin direction and, with respect to the KH-unstable regions predicted from the global magnetospheric geometry, help to identify the likely source region(s) of the wave activity.

[61] Consider a physical quantity, such as one aspect of wave activity or the layer thickness. If this quantity is controlled by the size of the source region and/or initial growth rate of remote production, it is expected to peak, like the growth rate [F98], at a given geomagnetic latitude for a specific clock angle. A dependence of the wave activity on clock angle and latitude would therefore represent another signature of remote KH waves, even more so at places on the flank magnetopause where the KH instability conditions are not satisfied with local input values. What is more, the same dependence on the LLBL thickness would constitute evidence for the contribution of the KH mechanism to the widening and perhaps the overall formation of the LLBL. To be precise, one expects a dependence in the latitude relative to the effective equatorial plane, taking account of the actual direction of the solar wind and the transverse warping of the tail current sheet on the flank [e.g., *Tsyganenko and Fairfield*, 2004].

5.4. Comparison Between Time Intervals: A Survey of the Parameter Space

[62] The comparison between time intervals, presenting different wave activity and subject to different local or global conditions, may help to identify the processes controlling the perturbations. Figures 9a and 9b show the global wavelet power spectra of magnetic field and of temperature time series for each of the five clock angle intervals, with the respective clock angle time series shown in the plot underneath (Figure 9c). Between the magnetic and plasma data sets, there is more variability in the periods (ii) and (iii) associated with the spectral peaks than there is for the dominant periods (i) near 200 s. Between time intervals, although those periods (i) behave roughly the same in the magnetic and plasma data sets, the spectral power in the magnetic field and the temperature behave differently, pointing to a difference in the cause of the magnetic and temperature perturbations.

[63] We need to find the best correlations between parameters characterizing each time interval to help us deduce the underlying phenomenology. We examine here: (1) the relationship between wave activity and IMF clock angle, (2) the relationship between wave activity and EBL thickness, (3) the relationship between IMF clock angle and EBL thickness, and (4) if possible the relationship between all three aspects in latitude. A selection of correlation plots between wave activity parameters at C2, GSM latitude, IMF clock angle and thickness is shown in Figure 10. Parameters for period E, where wave activity is nearly absent, are included for completeness. We also include and discuss some of the results pertaining to latitude, despite the small range available and without correcting for the actual direction of the solar wind or the transverse warping of the tail current sheet on the flank.

[64] First, we test the relation between wave activity, IMF clock angle and latitude. Figure 10a shows that the wavelengths λ for each dominant spectral peak, in particular the ones in the (i) range, generally increase with lower IMF clock angle. The left-hand plot of Figure 10b, correlating maximum power in the (i) range for the magnetic field time series with IMF clock angle, indicates that the increasing
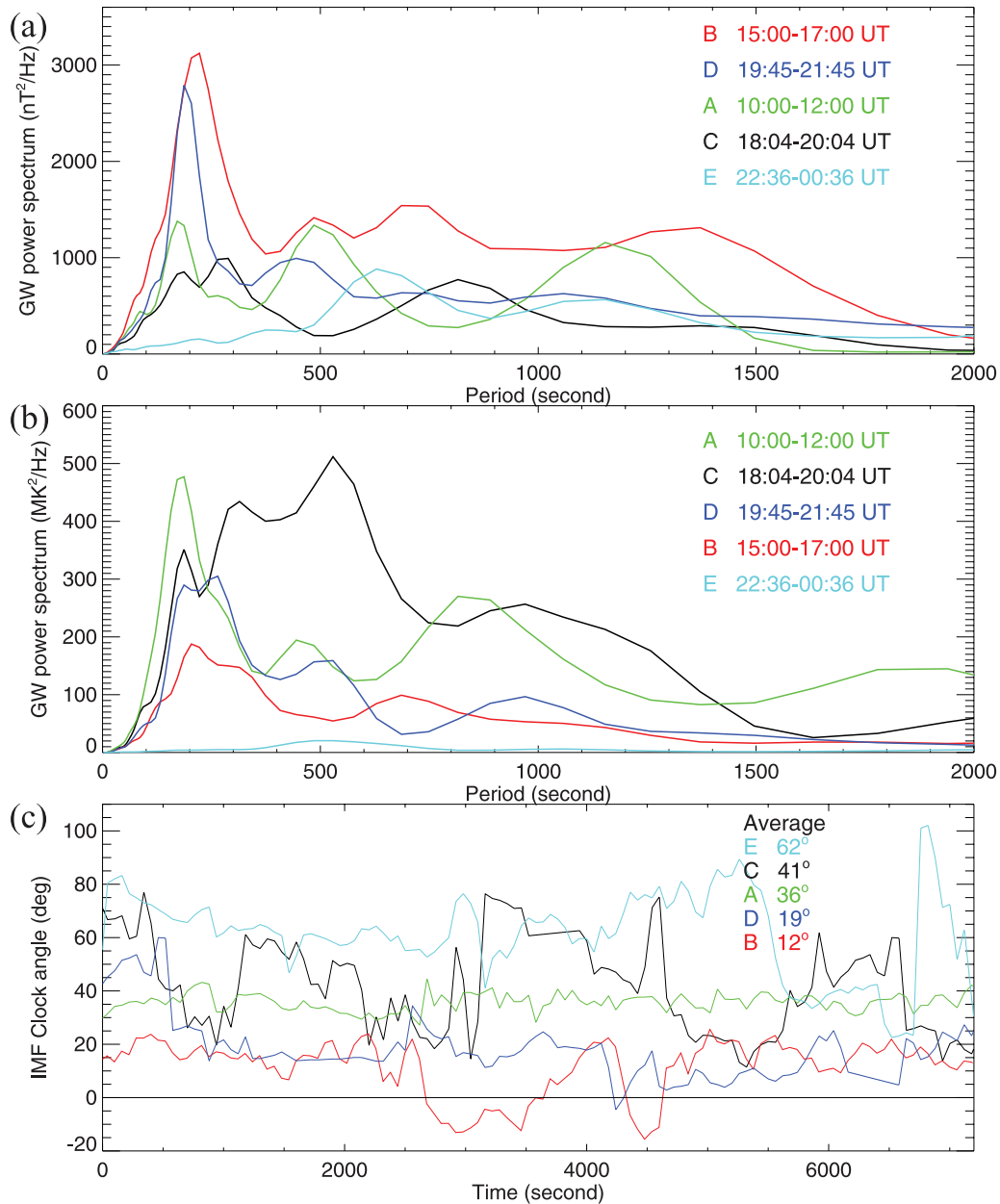
Figure 9. Comparison of spectral wave activity at C2 between five time intervals (of two-hour duration each). (a) Global wavelet power spectrum from magnetic field time series. (b) Global wavelet power spectrum from perpendicular electron temperature. (c) IMF clock angle for each of the five time intervals.

spectral power in the magnetic field correlates well with the decreasing clock angle. Therefore we conclude that the IMF clock angle is a major factor controlling both amplitudes and wavelengths of magnetic field fluctuations. Moreover, the observed North-South deviation angles θ_k indicate waves travelling generally with a southward component. For sampling locations on the dusk flank and in the southern magnetic hemisphere, the southward components in this event are qualitatively consistent with waves originating from upstream KH-unstable source regions with small positive IMF clock angle (see Figure 1b). The above results are consistent with the predicted IMF clock angle control of remote waves (section 5.3). In the left-hand plot of Figure 10c, it appears that the steepness angle of the leading edge,

with steeper wavefronts for small values of $\phi_k = |\phi_{k,b}|$, depends on the clock angle: apart from period E, the wavefronts tend to become less steep for lower clock angle. This behavior is inverse to the one expected from remote waves solely controlled by the IMF clock angle. In the center plots of Figures 10b and 10c, there are not enough points to show any latitude dependency of either (Figure 10b) the maximum power in the magnetic field time series for the periods (i) or (Figure 10c) the southward component of the wavefront, characterized by negative θ_k angle. Nevertheless, considering that the upper two points in Figure 10b have low clock angle and the lower points have larger clock angle, we note a hint of a dependence of the power in the magnetic field
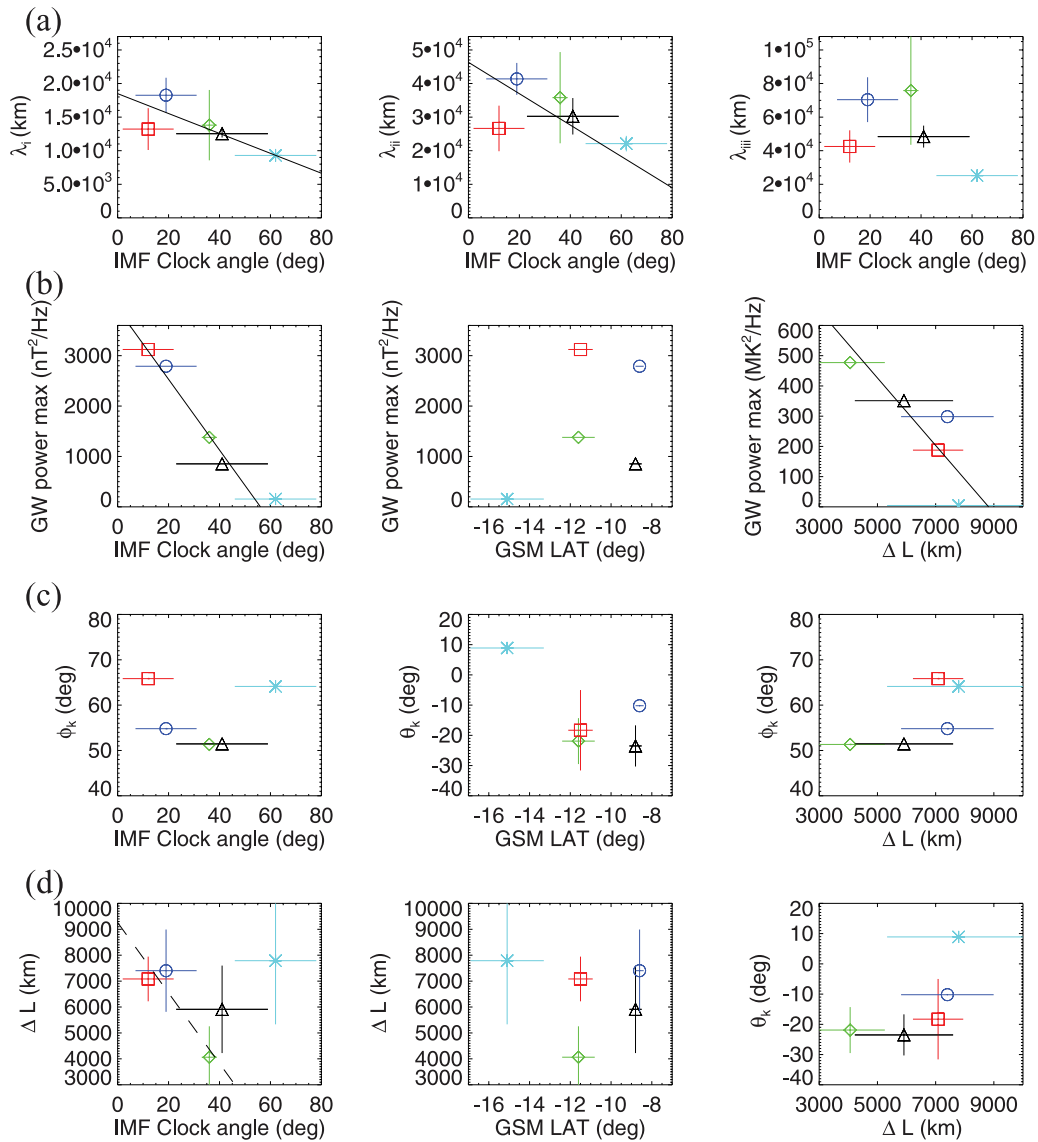
Figure 10. Correlation between wave activity parameters at C2, GSM latitude, IMF clock angle and thickness, ΔL, for five time intervals (of two-hour duration each) referred as (green diamond) A, (red square) B, (black triangle) C, (blue circle) D, and (cyan asterisk) E. The first row (Figure 10a) shows the wavelengths λ for each dominant spectral peak, from left to right, in the range (i) $4-10$ mHz, (ii) $1.6-2.9$ mHz, and (iii) below 1.6 mHz, versus IMF clock angle. The next three rows (Figures 10b, 10c, and 10d) show parameters versus (left) IMF clock angle, (center) GSM latitude, and (right) ΔL. Those parameters are: (b) the global wavelet maximum power in the (i) range for (left, center) magnetic field and (right) temperature, (c) direction angles: (left, right) steepness angle, ϕ_k, of the leading front and (center) North-South deviation angle, θ_k, average of elevation angles from leading and trailing fronts, and (d) (left, center) ΔL and (right) θ_k.

with latitude, which would peak at a preferred latitude depending on the clock angle.

[65] Second, we test the relation between wave activity and layer thickness, ΔL. The right-hand plot of Figure 10b shows that the increasing spectral power in the temperature for the periods (i) correlates with the decreasing thickness. This result suggests that for thicker layers, the plasma is less subject to perturbations. Although the periods or wavelengths are the same for plasma and magnetic fluctuations and may well indicate remote activity controlled by the IMF clock angle, our findings suggest that the amplitude pertur-

bations in plasma temperature vary with the local thickness (they increase as the layer thickness decreases). The local conditions, here, are not generally favorable for the KH instability to occur, i.e., for the local production of KH waves (section 5.1). Thus the inverse dependence noted above (between amplitude perturbations in plasma temperature and EBL thickness) represents one possible signature that the local conditions influence the properties of remotely generated waves. Since the magnetic wave activity is characterized with the largest component $B(m)$ of the magnetic field, amplitude variations in this tailward com-

ponent relate to wavelength changes (due to the tailward component stretching in the wave propagation direction along the unperturbed boundary in the *lm*-plane) and hence differ from the amplitude variations in plasma temperature (principally due to motions normal to the unperturbed boundary). In the right-hand plots of Figures 10c and 10d, we note that the steepening and the southward component of the wavefront (characterized by small ϕ_k and negative θ_k angles respectively) are stronger for thin layers. In this context, we speculate that a thin layer could be a favorable factor for preserving the propagation direction and steepening of the remote waves.

[66] Finally, we test the relation between EBL thickness, IMF clock angle and latitude. The center plot of Figure 10d shows the layer profile with latitude, varying with time as the clock angle changes and as the layer develops. Excluding period E, there is a tendency for the layer to be thicker toward the low latitudes and for this layer profile to increase as the clock angle decreases. In the left-hand plot of Figure 10d, the thickness estimates are shown versus clock angle. At low latitudes between 8 and 12°, there is a tendency for the layer to be thicker in periods of lower clock angles, with a linear fit (to four points) converging at the thickness of 9261 ± 3450 km for zero clock angle. On the basis of the confirmed relationship between clock angle and magnetic wave activity, as expected when generated by the KH mechanism, those results support, despite the limited number of points in the parameter space, the contributing role of the KH mechanism in the widening of the EBL.

6. Summary and Conclusions

[67] Identifying where KH activity is generated on the magnetopause and how it evolves is important if we are to understand how the KH mechanism contributes to the overall formation of the LLBL during northward IMF. Rolled-up vortices may be the sites of enhanced diffusion on closed field lines or sites where magnetic fields reconnect, allowing the transport of particles from the magnetosheath to the magnetosphere, necessary to explain the mixing of plasma in the LLBL. Although theories of particle transport in KH vortices are open to model developments, our use of ideal MHD theoretical studies of the KH instability [F98] to interpret observations is relevant to understanding the source and the nonlinear development of the waves. This is done here for the first time in an analysis of waves in the Pc5 (1–10 mHz) range, propagating near the dusk flank magnetopause, as observed at *Cluster* for an exceptionally prolonged period of time.

[68] In section 2, a good alignment of solar wind conditions with observations at the flank is obtained by cross-correlation of the clock angle in the magnetosheath with the IMF clock angle inferred at the bow shock nose. The propagation delays obtained are used to identify 2-hour intervals over which averages can be assumed reliable for representing solar wind conditions adjacent to the magnetopause. A time evolution of the boundary layer thickness, or "thickening", is difficult to obtain with single spacecraft or with multi-spacecraft that have separations smaller than the layer thickness. In section 3, to infer the boundary layer thickness when spacecraft separations are not large enough to simultaneously sample both outer sides of the boundary layer, we develop a new technique, which extends the transition parameter (TP) technique as follows: we correlate the TP (found from the relationship between the electron number density and the electron temperature) with the normal distances to the magnetopause, derived from two empirical solar-wind-driven models; the correlation factor is used to infer the temporal evolution of the thickness for a locally sampled layer. To characterize the evolution of the wave activity with changes in interplanetary magnetic field orientation, thickness of the boundary layer and geomagnetic latitude, we compare the latter conditions with wave activity parameters, such as power, wavelength, wavefront steepness and direction of propagation. The wave activity is characterized from magnetic field and temperature fluctuations, combining, in an unconventional fashion, power spectra and four-spacecraft timing at *Cluster* (section 4).

[69] Our key results can be summarized as follows.

[70] 1. We produce the first TP profiles, across the dusk flank boundary layer, of the magnitude and boundary normal components of magnetic and ion velocity fields. They are obtained with *Cluster* and are complementary to profiles from scatterplots of *Wind* spacecraft crossings in this plasma region [*Phan et al.*, 1997].

[71] 2. Using observations made simultaneously at *Geotail* on the dayside and *Cluster* tailward of the terminator, we confirm the broadening of the electron boundary layer with distance along the flank, obtained previously statistically by *Mitchell et al.* [1987].

[72] 3. We report 3-wavelength (or 3-length-scale) KH structures, with wavefront steepness and propagation direction consistent with the characteristics of remotely generated waves.

[73] 4. In the event under study, local production of KH activity is not generally expected to occur, nor it is expected to dominate. In particular, we show that one strong stabilizing effect may be due to the IMF field lines being caught up and dragged sunward by the surface waves.

[74] 5. For the first time in space, we find evidence for an inverse dependence between clock angle and wavelength at the flank, as expected when generated by the KH mechanism. Hence, this result, originally predicted by the model of F98, confirms the significance of source regions and nonlinear development for interpreting observations of remotely generated KH waves. Given the inverse dependence between the geomagnetic pulsation period and the IMF clock angle previously shown by *Farrugia et al.* [2000], our results point to a mechanism whereby varying degrees of wave activity at the magnetopause regulate the geomagnetic pulsation periods.

[75] 6. We find that the local layer thickness influences the properties of remotely generated waves in their amplitude, wavefront steepness and direction of propagation.

[76] 7. Finally, we provide evidence of the contribution of the KH mechanism to the widening of the electron LLBL. As the LLBL thickening may in turn stabilize the surface waves, the thicker layers forming at low IMF clock angle may explain the changes in wave properties with lower IMF clock angle.

[77] To characterize the evolution of the KH activity with changes in interplanetary and local conditions and along the flank magnetopause, we advocate the use of multi-spacecraft and distant locations for comparisons. We reviewed a

number of expected signatures, which can be further tested with more observations. An unprecedented number of satellites is now or has recently been crossing the Earth's magnetospheric boundary in concert, repeatedly and in different places (the 4 *Cluster*, the Double Star TC-1 satellite and other spacecraft such as *Geotail* and the 5 THEMIS spacecraft). In favorable configurations, these spacecraft are separated from each other by several Earth radii along the flank magnetopause. Together with the recent increase of the *Cluster* satellite separations, they provide the opportunity to confirm our results and extend the methods demonstrated in this study. At separations large enough to simultaneously sample both inner and outer edges of the boundary layer, they may help to validate the technique developed here (using the TP) for inferring the electron boundary layer thickness. Features interpreted as rolled-up vortices have been reported in the event analyzed [*Hasegawa et al.*, 2004]. Our treatment of the oscillatory structures as waves can be improved, for instance, with a characterization of the vorticity in those structures.

[79] Zuyin Pu thanks the reviewers for their assistance in evaluating this paper.

References

Antonova, E. E. (2005), The structure of the magnetospheric boundary layers and the magnetospheric turbulence, *Planet. Space Sci.*, *53*, 161–168, doi:10.1016/j.pss.2004.09.041.

Bai, T., and E. W. Cliver (1990), A 154 day periodicity in the occurrence rate of proton flares, *Astrophys. J.*, *363*, 299–309, doi:10.1086/169342.

Balogh, A., et al. (2001), The Cluster magnetic field investigation: Overview of in-flight performance and initial results, *Ann. Geophys.*, *19*, 1207–1217.

Belmont, G., and G. Chanteur (1989), Advances in magnetopause Kelvin-Helmholtz instability studies, *Phys. Scr.*, *40*, 124–128.

Bogdanova, Y. V., et al. (2005), On the formation of the high-altitude stagnant cusp: Cluster observations, *Geophys. Res. Lett.*, *32*, L12101, doi:10.1029/2005GL022813.

Chandrasekhar, S. (1961), *Hydrodynamic and Hydromagnetic Stability*, International Series of Monographs on Physics, Clarendon, Oxford.

Crooker, N. U., J. G. Luhmann, C. T. Russell, E. J. Smith, J. R. Spreiter, and S. S. Stahara (1985), Magnetic field draping against the dayside magnetopause, *J. Geophys. Res.*, *90*, 3505–3510.

de Keyser, J. (2005), The Earth's magnetopause: Reconstruction of motion and structure, *Space Sci. Rev.*, *121*, 225–235, doi:10.1007/s11214-006-6731-3.

Dungey, J. W. (1961), Interplanetary magnetic field and the auroral zones, *Phys. Rev. Lett.*, *6*, 47–48, doi:10.1103/PhysRevLett.6.47.

Eastman, T. E., E. W. Hones, S. J. Bame, and J. R. Asbridge (1976), The magnetospheric boundary layer: Site of plasma, momentum and energy transfer from the magnetosheath into the magnetosphere, *Geophys. Res. Lett.*, *3*, 685–688.

Elphic, R. C., and C. T. Russell (1979), ISEE-1 and 2 magnetometer observations of the magnetopause, in *Proc. Magnetospheric Boundary Layers Conf.*, edited by J. Lemaire and B. Battrick, pp. 43–50, ESA, Alpbach, SP-148.

Fairfield, D. H. (1967), The ordered magnetic field of the magnetosheath, *J. Geophys. Res.*, *72*, 5865–5877.

Fairfield, D. H., A. Otto, T. Mukai, S. Kokubun, R. P. Lepping, J. T. Steinberg, A. J. Lazarus, and T. Yamamoto (2000), Geotail observations of the Kelvin-Helmholtz instability at the equatorial magnetotail boundary for parallel northward fields, *J. Geophys. Res.*, *105*, 21,159–21,173.

Farrugia, C. J., F. T. Gratton, L. Bender, H. K. Biernat, N. V. Erkaev, J. M. Quinn, R. B. Torbert, and V. Dennisenko (1998), Charts of joint Kelvin-Helmholtz and Rayleigh-Taylor instabilities at the dayside magnetopause for strongly northward interplanetary magnetic field, *J. Geophys. Res.*, *103*, 6703–6727.

Farrugia, C. J., et al. (2000), Coordinated wind, interball/tail, and ground observations of Kelvin-Helmholtz waves at the near-tail, equatorial magnetopause at dusk: January 11, 1997, *J. Geophys. Res.*, *105*, 7639–7667.

Farrugia, C. J., F. T. Gratton, and R. B. Torbert (2001), Viscous-type processes in the solar wind-magnetosphere interaction, *Space Sci. Rev.*, *95*, 443–456.

Foullon, C., E. Verwichte, and V. M. Nakariakov (2004), Detection of ultra-long-period oscillations in an EUV filament, *Astron. Astrophys.*, *427*, L5–L8, doi:10.1051/0004-6361:200400083.

Foullon, C., E. Verwichte, V. M. Nakariakov, and L. Fletcher (2005), X-ray quasi-periodic pulsations in solar flares as magnetohydrodynamic oscillations, *Astron. Astrophys.*, *440*, L59–L62, doi:10.1051/0004-6361:200500169.

Frank, L. A., K. L. Ackerson, W. R. Paterson, J. A. Lee, M. R. English, and G. L. Pickett (1994), The comprehensive plasma instrumentation (CPI) for the Geotail spacecraft, *J. Geomagn. Geoelectr.*, *46*, 23.

Fujimoto, M., and T. Terasawa (1994), Anomalous ion mixing within an MHD scale Kelvin-Helmholtz vortex, *J. Geophys. Res.*, *99*, 8601–8613.

Fuller, W. A. (1995), *Introduction to Statistical Time Series*, John Wiley, Hoboken, N. J.

Gnavi, G., F. T. Gratton, C. J. Farrugia, and L. Bilbao (2006), The KH stability of the supersonic magnetopause flanks modeled by continuous profiles for the transition, in *Plasma and Fusion Science: 16th IAEA Technical Meeting on Research using Small Fusion Devices*, *American Institute of Physics Conference Series*, vol. 875, edited by J. Julio and E. Herrera Velazquez, pp. 296–299, AIP, Mexico City, Mexico, doi:10.1063/1.2405952.

Gustafsson, G., et al. (2001), First results of electric field and density observations by Cluster EFW based on initial months of operation, *Ann. Geophys.*, *19*, 1219–1240.

Hapgood, M. A., and D. A. Bryant (1990), Re-ordered electron data in the low-latitude boundary layer, *Geophys. Res. Lett.*, *17*, 2043–2046.

Hapgood, M. A., and D. A. Bryant (1992), Exploring the magnetospheric boundary layer, *Planet. Space Sci.*, *40*, 1431–1459, doi:10.1016/0032-0633(92)90099-A.

Hasegawa, H., M. Fujimoto, T.-D. Phan, H. Rème, A. Balogh, M. W. Dunlop, C. Hashimoto, and R. TanDokoro (2004), Transport of solar wind into Earth's magnetosphere through rolled-up Kelvin-Helmholtz vortices, *Nature*, *430*, 755–758, doi:10.1038/nature02799.

Horne, J. H., and S. L. Baliunas (1986), A prescription for period analysis of unevenly sampled time series, *Astrophys. J.*, *302*, 757–763, doi:10.1086/164037.

Hughes, W. J. (1981), Magnetospheric ULF waves: A tutorial with a historical perspective, in *Solar Wind Sources of Magnetospheric Ultra-Low-Frequency Waves*, *Geophys. Monogr. Ser.*, vol. 81, edited by M. J. Engebretson, K. Takahashi, and M. Scholer, AGU, Washington, DC.

Johnstone, A. D., et al. (1997), Peace: A plasma electron and current experiment, *Space Sci. Rev.*, *79*, 351–398.

King, J. H., and N. E. Papitashvili (2005), Solar wind spatial scales in and comparisons of hourly Wind and ACE plasma and magnetic field data, *J. Geophys. Res.*, *110*, A02104, doi:10.1029/2004JA010649.

Kivelson, M. G., and S.-H. Chen (1995), The magnetopause: Surface waves and instabilities and their possible dynamical consequences, in *Physics of the Magnetopause*, *Geophys. Monogr. Ser.*, vol. 90, edited by P. Song, B. U. Ö. Sonnerup, and M. F. Thomsen, AGU, Washington, D. C.

Kokubun, S., T. Yamamoto, M. H. Acuna, K. Hayashi, K. Shiokawa, and H. Kawano (1994), The Geotail magnetic field investigation, *J. Geomagn. Geoelectr.*, *46*, 7.

Lepping, R. P., and L. F. Burlaga (1979), Geomagnetopause surface fluctuations observed by Voyager 1, *J. Geophys. Res.*, *84*, 7099–7106.

Lockwood, M., and M. A. Hapgood (1997), How the magnetopause transition parameter works, *Geophys. Res. Lett.*, *24*, 373–376.

Manuel, J. R., and J. C. Samson (1993), The spatial development of the low-latitude boundary layer, *J. Geophys. Res.*, *98*, 17,367–17,386.

McComas, D. J., S. J. Bame, P. Barker, W. C. Feldman, J. L. Phillips, P. Riley, and J. W. Griffee (1998), Solar Wind Electron Proton Alpha Monitor (SWEPAM) for the advanced composition explorer, *Space Sci. Rev.*, *86*, 563–612.

Mitchell, D. G., F. Kutchko, D. J. Williams, T. E. Eastman, and L. A. Frank (1987), An extended study of the low-latitude boundary layer on the dawn and dusk flanks of the magnetosphere, *J. Geophys. Res.*, *92*, 7394–7404.

Miura, A. (1984), Anomalous transport by magnetohydrodynamic Kelvin-Helmholtz instabilities in the solar wind-magnetosphere interaction, *J. Geophys. Res.*, *89*, 801–818.

Miura, A. (1995), Dependence of the magnetopause Kelvin-Helmholtz instability on the orientation of the magnetosheath magnetic field, *Geophys. Res. Lett.*, *22*, 2993–2996.

Miura, A. (1999a), A quantitative test of the self-organization hypothesis of the magnetopause Kelvin-Helmholtz instability as an inverse problem, *Geophys. Res. Lett.*, *26*, 409–412.

Miura, A. (1999b), Self-organization in the two-dimensional magnetohydrodynamic transverse Kelvin-Helmholtz instability, *J. Geophys. Res.*, *104*, 395–411.

Miura, A., and P. L. Pritchett (1982), Nonlocal stability analysis of the MHD Kelvin-Helmholtz instability in a compressible plasma, *J. Geophys. Res.*, *87*, 7431–7444.

Øieroset, M., T. D. Phan, M. Fujimoto, L. Chan, R. P. Lin, and R. Skoug (2002), Spatial and temporal variations of the cold dense plasma sheet: Evidence for a low-latitude boundary layer source?, in *Earth's Low-Latitude Boundary Layer*, *Geophys. Monogr. Ser.*, vol. 133, edited by P. T. Newell and T. Onsager, AGU, Washington, D. C.

Otto, A., and D. H. Fairfield (2000), Kelvin-Helmholtz instability at the magnetotail boundary: MHD simulation and comparison with Geotail observations, *J. Geophys. Res.*, *105*, 21,175–21,190.

Owen, C. J., M. G. G. T. Taylor, I. C. Krauklis, A. N. Fazakerley, M. W. Dunlop, and J. M. Bosqued (2004), Cluster observations of surface waves on the dawn flank magnetopause, *Ann. Geophys.*, *22*, 971–983.

Phan, T. D., et al. (1997), Low-latitude dusk flank magnetosheath, magnetopause, and boundary layer for low magnetic shear: Wind observations, *J. Geophys. Res.*, *102*, 19,883–19,895.

Rème, H., et al. (2001), First multispacecraft ion measurements in and near the Earth's magnetosphere with the identical Cluster ion spectrometry (CIS) experiment, *Ann. Geophys.*, *19*, 1303–1354.

Roelof, E. C., and D. G. Sibeck (1993), Magnetopause shape as a bivariate function of interplanetary magnetic field B_z and solar wind dynamic pressure, *J. Geophys. Res.*, *98*, 21,421–21,450.

Russell, C. T., M. M. Mellott, E. J. Smith, and J. H. King (1983), Multiple spacecraft observations of interplanetary shocks: Four spacecraft determination of shock normals, *J. Geophys. Res.*, *88*, 4739–4748.

Scargle, J. D. (1982), Studies in astronomical time series analysis. II: Statistical aspects of spectral analysis of unevenly spaced data, *Astrophys. J.*, *263*, 835–853, doi:10.1086/160554.

Schwartz, S. J. (1998), Shock and Discontinuity Normals, Mach Numbers, and Related Parameters, in *Analysis Methods for Multi-Spacecraft Data*, edited by G. Pashmann and P. W. Daly, chap. 10, pp. 249–270, ISSI Scientific Report SR-001, Bern.

Shue, J.-H., J. K. Chao, H. C. Fu, C. T. Russell, P. Song, K. K. Khurana, and H. J. Singer (1997), A new functional form to study the solar wind control of the magnetopause size and shape, *J. Geophys. Res.*, *102*, 9497–9512.

Smith, C. W., J. L'Heureux, N. F. Ness, M. H. Acuña, L. F. Burlaga, and J. Scheifele (1998), The ACE Magnetic Fields Experiment, *Space Sci. Rev.*, *86*, 613–632.

Song, P., and C. T. Russell (2002), Flow in the magnetosheath: The legacy of John Spreiter, *Planet. Space Sci.*, *50*, 447–460.

Song, P., C. T. Russell, and M. F. Thomsen (1992), Slow mode transition in the frontside magnetosheath, *J. Geophys. Res.*, *97*, 8295–8305.

Song, P., C. T. Russell, T. I. Gombosi, and D. L. DeZeeuw (2002), A model of the formation of the low-latitude boundary layer for northward IMF by reconnection: A summary and review, in *Earth's Low-Latitude Boundary Layer*, *Geophys. Monogr. Ser.*, vol. 133, edited by P. T. Newell and T. Onsager, AGU, Washington, D. C.

Starck, J.-L., and F. Murtagh (2002), *Astronomical Image and Data Analysis*, Astron. and Astrophys. Library, Springer, Berlin.

Talwar, S. P. (1964), Hydromagnetic stability of the magnetospheric boundary, *J. Geophys. Res.*, *69*, 2707–2713.

Terasawa, T., et al. (1997), Solar wind control of density and temperature in the near-Earth plasma sheet: WIND/GEOTAIL collaboration, *Geophys. Res. Lett.*, *24*, 935–938, doi:10.1029/96GL04018.

Thomas, V. A., and D. Winske (1993), Kinetic simulations of the Kelvin-Helmholtz instability at the magnetopause, *J. Geophys. Res.*, *98*, 11,425–11,438.

Torrence, C., and G. P. Compo (1998), A practical guide to wavelet analysis, *Bull. Am. Meteorol. Soc.*, *79*(1), 61–78, 79, 61–78.

Treumann, R. A., J. Labelle, and T. M. Bauer (1995), Diffusion processes: An observational perspective, in *Physics of the Magnetopause*, *Geophys. Monogr. Ser.*, vol. 90, edited by P. Song, B. U. Ö. Sonnerup, and M. F. Thomsen, AGU, Washington, D. C.

Tsyganenko, N. A., and D. H. Fairfield (2004), Global shape of the magnetotail current sheet as derived from Geotail and Polar data, *J. Geophys. Res.*, *109*, A03218, doi:10.1029/2003JA010062.

Walker, A. D. M. (1981), The Kelvin-Helmholtz instability in the low-latitude boundary layer, *Planet. Space Sci.*, *29*, 1119–1133, doi:10.1016/0032-0633(81)90011-8.

Wu, C. C. (1986), Kelvin-Helmholtz instability at the magnetopause boundary, *J. Geophys. Res.*, *91*, 3042–3060.

————————————

C. J. Farrugia and R. B. Torbert, Space Science Center and Department of Physics, University of New Hampshire, 9 College Rd., Durham, NH 03824, USA.

A. N. Fazakerley, C. Foullon, and C. J. Owen, Mullard Space Science Laboratory, University College London, Holmbury St Mary, Dorking, Surrey RH5 6NT, UK. (cf2@mssl.ucl.ac.uk)

F. T. Gratton, Instituto de Física del Plasma, CONICET, Universidad de Buenos Aires, Pab. 1, 1428, Buenos Aires, Argentina.